日本磁気学会
ISSN 2432-0250
Journal of the Magnetics Society of Japan
Electronic Journal URL: https://www.jstage.jst.go.jp/browse/msjmag

Vol.43 No.2 2019

Journal

Thin Films, Fine Particles, Multilayers, Superlattices

Biomagnetism / Medical Applications

JOURNAL OF THE MAGNETICS SOCIETY OF JAPAN

Vol.43 No.2 2019

日本磁気学会

ISSN 2432-0250

HP: http://www.magnetics.jp/ e-mail: msj@bj.wakwak.com

Electronic Journal: http://www.jstage.jst.go.jp/browse/msjmag

Journal of the Magnetics Society of Japan
Vol. 43, No. 2

Electronic Journal URL: https://www.jstage.jst.go.jp/browse/msjmag

CONTENTS

J. Magn. Soc. Jpn., **43**, 17-20 (2019)

Letter

Fabrication of noncentrosymmetric Nb/V/Ta superlattice and its superconductivity

F. Ando[1], D. Kan[1], Y. Shiota[1], T. Moriyama[1], Y. Shimakawa[1,2], and T. Ono[1,3]

[1]Institute for Chemical Research, Kyoto University, *Gokasho Uji, Kyoto 611-0011, Japan*

[2]Integrated Research Consortium on Chemical Sciences, Kyoto University, *Gokasho Uji, Kyoto 611-0011, Japan*

[3]Center for Spintronics Research Network (CSRN), Graduate School of Engineering Science, Osaka University, *1-3 Machikaneyama-cho Toyonaka, Osaka 560-8531, Japan*

Nb, V, and Ta are all well-known superconducting elements in a simple substance. We report the superconductivity of Nb/V/Ta superlattices sputtered onto MgO(100) substrates, in which global inversion symmetry was broken along the stacking direction. It was found that the superlattices had long-range crystalline coherence with the well-defined periodicity of the constituent layers, and they exhibited superconducting transition despite the thicknesses of the layers.

Keywords: inversion symmetry breaking, artificial superlattice, epitaxial film, X-ray 2θ/θ measurement, superconductivity

1. Introduction

In recent years, spin-orbit interaction (SOI) has been attracted intense attentions in the various fields of solid state physics, such as spintronics[1)–3)], topological matter[4)], and unconventional superconductivity[5)]. In the presence of inversion symmetry breaking, SOI entangles the spin and orbit degrees of freedom in the electron system and enables the mutual control of electronic and spin properties. In case of superconductors, the SOI with broken inversion symmetry significantly forbids the conventional classification of Cooper pairs[5)]. Instead, a new pairing symmetry, i.e., a mixed spin singlet-triplet state, is expected to be realized[6),7)]. There have been several reports of the noncentrosymmetric superconductors where the crystal structure lacks a center of inversion, such as $CePt_3Si$[8)], $CeRhSi_3$[9),10)] , and UIr[11)].

Recently, Rashba effect on two-dimensional (2D) superconductivity was studied using d-wave heavy fermion superconductor $CeCoIn_5$ sandwiched by two different nonmagnetic metals[12)]. This previous work reveals that Rashba effect controlled in the tricolor structure exerts profound changes in the 2D superconducting properties as theoretically pointed out[13),14)]. The finding naturally leads us to an expectation that an exotic superconductivity can be explored in 3D artificially engineered superlattice using three kinds of superconductors A, B, and C. As shown in Fig. 1(a), global inversion symmetry is broken in *ABC*-type superlattice and we can easily tune Rashba effect yielded by asymmetric potential gradient ∇V.

In this study, we at first investigate the growth and conductivity of *ABC*-type superlattices as a new platform to investigate an exotic superconductivity. We choose Nb, V, and Ta as the constituent layers, which are all commonly-used superconducting elements and have body-centered cubic (bcc) lattice structure[15)–19)].

2. Experimental Procedure

The film deposition was carried out by d.c. magnetron sputtering in an high vacuum system at a base pressure of 1.0×10^{-5} Pa or better. Ar was used as sputter gas. Prior to film growth, the MgO(100) substrate was washed with acetone and heated at 600 °C for 30 minutes in the sputtering chamber to drive off impurities. Figure 1(b) shows a design of the superlattice structure. Nb, V, and Ta layers of the thickness t were repetitively sputtered onto the MgO substrate. The deposition rates were kept constant at 0.35, 0.21, and 0.44 Å/s for Nb, V, and Ta, respectively. The MgO substrate was heated at 750 °C during the deposition as well as the previous report[17)]. We changed the thickness t from 1.0 nm to 5.0 nm while fixing the total thickness to be 60 nm. We can expect that Rashba effect on the superconductivity can be controlled by tuning the thickness t. A 3 nm thick Pt layer deposited at room temperature prevents the oxidation.

To confirm the epitaxial growth of Nb/V/Ta superlattices, reflection high-energy electron diffraction (RHEED) patterns were observed *in-situ* before and after the deposition of the superlattices. The electron beam was injected along the MgO[100] and MgO[110] azimuthal directions. Figure 1(b) shows the RHEED patterns of MgO substrate (1st) and Nb/V/Ta superlattice for t = 1.0 nm (2nd). The observed patterns indicate an epitaxial growth of the bcc-Nb/V/Ta superlattice with Nb/V/Ta(100) on the MgO(100) substrate where Nb/V/Ta[100]‖MgO[100][20),21)]. The in-plane lattice constant of the top Ta surface is estimated to be 3.2 Å from the RHEED streak distance[22)]. This smaller lattice constant compared with that of bulk bcc-Ta (3.30 Å) can be accounted for by a lattice mismatch with the neighboring V layer. The similar RHEED patterns were observed for other films (t = 2.0 and 5.0 nm, [Nb (2.0)/V (2.0)/Ta (2.0)]×10 and [Nb (5.0)/V (5.0)/Ta (5.0)]×4).

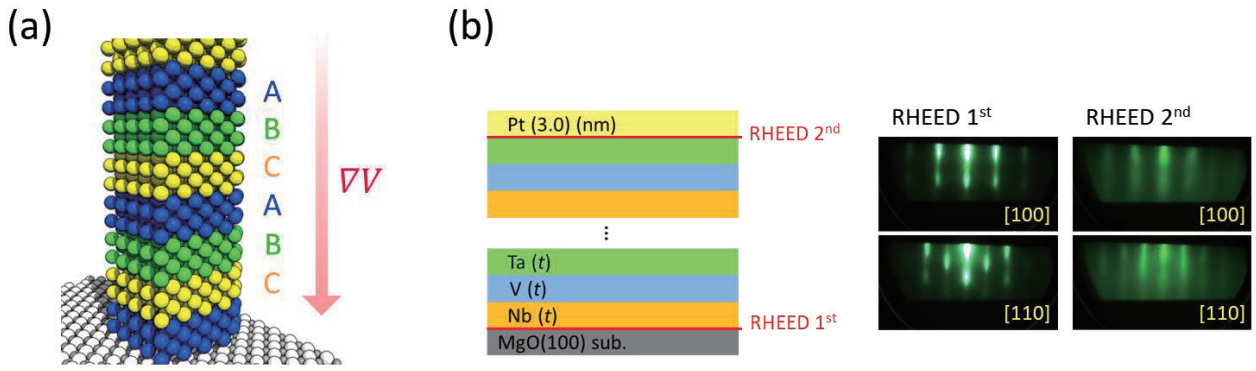

Fig. 1 (a) Schematic design of *ABC*-type superlattice. Red arrow represents asymmetric potential gradient ∇V due to global inversion symmetry breaking. (b) Film structure sputtered onto MgO (100) substrates. Nb, V, and Ta were chosen as constituent elements for *ABC*-type superlattice. RHEED streak patterns were observed before and after deposition of [Nb (1.0)/V (1.0)/Ta (1.0)]$_{20}$ superlattice. Electron beam was injected along the MgO[100] and MgO[110] azimuthal directions.

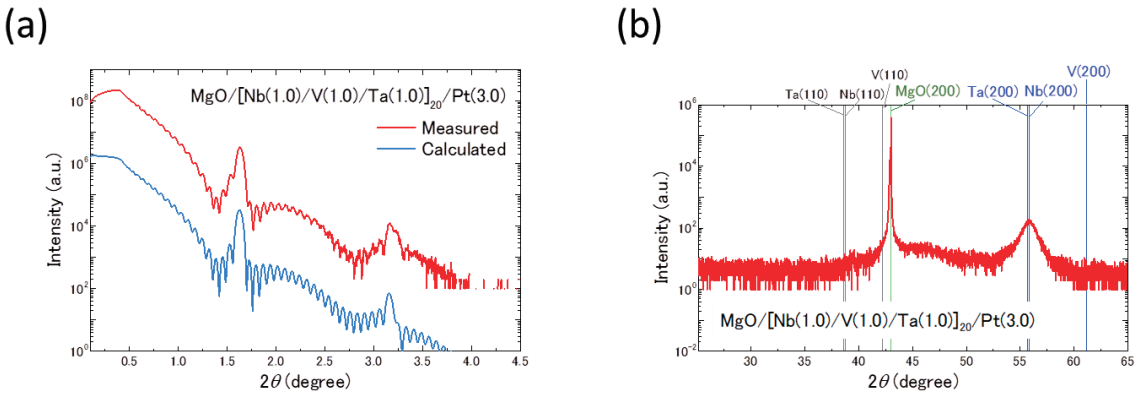

Fig. 2 X-ray 2θ/θ measurements for [Nb (1.0)/V (1.0)/Ta (1.0)]$_{20}$/Pt (3.0). (a) Measured (red) and calculated (blue) X-ray reflection curves identify interfacial morphology of superlattice. Two distinct fringes resulting from interference between periodic interfaces indicate highly sharp interfaces with almost no mixture. (b) X-ray diffraction scan was performed to identify crystalline structure of superlattice. Two sharp peaks corresponding to MgO(200) and Nb(200) [or Ta(200)] strongly indicate that superlattice was epitaxially grown with bcc lattice structure on MgO(100) substrate.

3. Results and Discussions

To investigate the interfacial morphology and crystalline structure of the superlattice, we performed X-ray 2θ/θ measurements[23] using Philips X'Pert MRD diffractometer with monochromatic CuK$_{\alpha 1}$ radiation. Figure 2(a) shows the measured and calculated X-ray reflection curves of the superlattice (t = 1.0 nm). The measured curve shows two noticeable Bragg peaks and Kiessig fringes[24]. From the series of the two peak-angles, it is directly found that the film has a characteristic length of 2.84 nm. This means that the 2.8-nm-thick Nb/V/Ta multi-layers are periodically deposited with highly sharp interfaces, which is a desirable construction to enhance Rashba effect. The measured curve was fitted as a function of thicknesses and roughness of Nb, V, and Ta layers using a Philips X'Pert reflectivity program. The calculated curve clearly reproduces two Bragg peaks and Kiessig fringes of the measured one. The calculated thicknesses of Nb, V, and Ta layers are 0.9, 1.0, and 0.9 nm, respectively, which almost agree with the original design of the superlattice. Mean values of the interfacial roughness obtained from the fit were equal to 0.4-0.9 nm (2-4 atomic layers).

Secondly, we performed the X-ray diffraction (XRD) scan for the same film (t = 1.0 nm). Figure 2(b) shows the obtained result of XRD scan. The expected angles of the peaks are calculated using lattice constants listed in the *American Institute of Physics Handbook*[22]. A distinct peak around 56° can be seen in the measured XRD curve, which corresponds to the expected one from bcc-Nb(200) or bcc-Ta(200). Together with the RHEED 2nd in Fig. 1(b), the XRD curve ensures the epitaxial growth of the deposited films with bcc lattice structure.

Finally, we conducted electric transport measurements to characterize the electrical conductivity at low

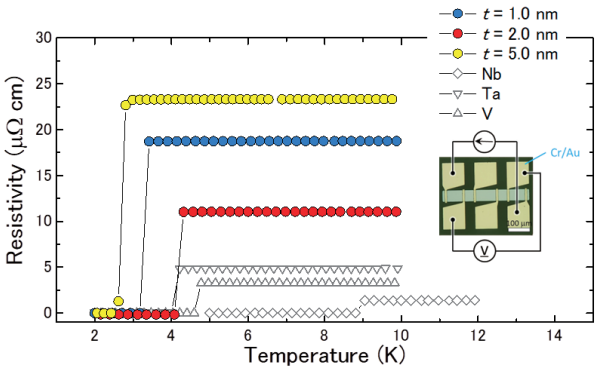

Fig. 3 Temperature dependence of electric resistivity in Nb/V/Ta superlattices (t = 1.0, 2.0, and 5.0 nm) and 120-nm-thick Nb, V, Ta single-layer films. Inset shows photomicrograph of processed film along with measurement configuration. All [Nb/V/Ta] superlattices exhibited abrupt drop in resistivity.

temperature. In order to enhance the 3D nature[25),26)], we fabricated the superlattices increasing the total thickness from 60 nm to 120 nm. Note that there is almost no difference in RHEED patterns by increasing the total thickness. The inset of Fig. 3(a) shows a photomicrograph of the processed film with the measurement configuration. The films were patterned into a 50-μm-wide wire structure by a conventional photolithography and Ar ion milling process. Then, Cr (5 nm)/Au (100 nm) electrodes were formed on the films using a resistance heating evaporation system and a lift-off process. Four-terminal measurements were performed to probe the temperature dependence of the sheet resistivity using the Physical Property Measurement System (PPMS-9T, Quantum Design). Figure 3(a) shows the measurement results for the superlattices (t = 1.0, 2.0, 5.0 nm) with those for 120-nm-thick Nb, V, Ta single layer films. The superlattices exhibit the superconducting transitions, whose temperatures T_C are comparable to those of Nb, V, Ta single layer films. However, the t dependence of the T_C is somehow strange because T_C among the superlattice (t = 2.0 nm) is the highest of the three films. We need further study about the physics behind the superconductivity.

4. Conclusion

We study the growth and superconductivity of Nb/V/Ta superlattices sputtered onto MgO(100) substrates. The RHEED patterns and X-ray 2θ/θ measurements reveal that the superlattices have long-range crystalline coherence and the well-defined periodicity of the constituent layers. Moreover, the superlattices exhibited superconducting transition comparable to the Nb, V, and Ta single layer films. The *ABC*-type noncentrosymmetric superlattice presented in this work will be a new platform for searching exotic superconductive properties[7),10),27)–30)].

Acknowledgements This work was supported by JSPS KAKENHI Grant Numbers 15H05702, 16H05977, 26103002, the Collaborative Research Program of the Institute for Chemical Research, Kyoto University, and the Cooperative Research Project Program of the Research Institute of Electrical Communication, Tohoku University.

References

1) S. Murakami, N. Nagaosa, and S. Zhang, *Science* **301**, 1348 (2003).
2) J. Sinova, D. Culcer, Q. Niu, N.A. Sinitsyn, T. Jungwirth, and A.H. Macdonald, *Phys. Rev. Lett.* **92**, 126603 (2004).
3) A. Fert, V. Cros, and J. Sampaio, *Nat. Nanotechnol.* **8**, 152 (2013).
4) X. Qi and S. Zhang, *Rev. Mod. Phys.* **83**, 1057 (2011).
5) E. Bauer and M. Sigrist, *Non-Centrosymmetric Superconductors: Introduction and Overview* (Springer-Verlag Berlin Heidelberg, 2012).
6) L.P. Gor'kov and E.I. Rashba, *Phys. Rev. Lett.* **87**, 37004 (2001).
7) P. Frigeri, D.F. Agterberg, A. Koga, and M. Sigrist, *Phys. Rev. Lett.* **92**, 097001 (2004).
8) E. Bauer, G. Hilscher, H. Michor, C. Paul, E.W. Scheidt, A. Gribanov, Y. Seropegin, H. Noël, M. Sigrist, and P. Rogl, *Phys. Rev. Lett.* **92**, 027003 (2004).
9) N. Kimura, K. Ito, K. Saitoh, Y. Umeda, H. Aoki, and T. Terashima, *Phys. Rev. Lett.* **95**, 247004 (2005).
10) N. Kimura, K. Ito, H. Aoki, S. Uji, and T. Terashima, *Phys. Rev. Lett.* **98**, 197001 (2007).
11) T. Akazawa, H. Hidaka, T. Fujiwara, T.C. Kobayashi, E. Yamamoto, Y. Haga, R. Settai, and Y. Onuki, *J. Phys. Condens. Matter* **16**, L29 (2004).
12) M. Naritsuka, T. Ishii, S. Miyake, Y. Tokiwa, R. Toda, M. Shimozawa, T. Terashima, T. Shibauchi, Y. Matsuda, and Y. Kasahara, *Phys. Rev. B* ***96***, 174512 (2017).
13) S. Fujimoto, *J. Phys. Soc. Jpn.* **76**, 051008 (2007).
14) D. Maruyama and Y. Yanase, *J. Phys. Soc. Jpn.* **84**, 074702 (2015).
15) B.Y. Jin and J.B. Ketterson, *Adv. Phys.* **38**, 189 (1989).
16) J.R. Rairden and C.A. Neugebauer, *Proc. IEEE* **52**, 1234 (1964).
17) S.M. Durbin, J.E. Cunningham, M.E. Mochel, and C.P. Flynn, *J. Phys. F Met. Phys.* **11**, L223 (1981).
18) P.R. Broussard and T.H. Geballe, *Phys. Rev.* B **35**, 1664 (1987).
19) M. Gutsche, H. Kraus, J. Jochum, B. Kemmather, and G. Gutekunst, *Thin Solid Films* **248**, 18 (1994).
20) D.B. Beringer, W.M. Roach, C. Clavero, C.E. Reece, and R.A. Lukaszew, *Phys. Rev. ST Accel. Beams* **16**, 022001 (2013).
21) G. Oya, M. Koishi, Y. Sawada, G. Oya, M. Koishi, and Y. Sawada, *J. Appl. Phys.* **60**, 1440 (1986).
22) D.E. Gray, *American Institute of Physics Handbook* (McGraw-Hill Book Company, Inc., New York, 1957).

23) W.J. Bartels, J. Hornstra, and D.J.W. Lobeek, in *Acta Crystallogr. Sect. A* (1986), pp. 409–588.
24) H. Zabel, *Appl. Phys.* A **58**, 159 (1994).
25) J.I. Kodama, M. Itoh, and H. Hirai, *J. Appl. Phys.* **54**, 4050 (1983).
26) A.I. Gubin, K.S. Il'in, S.A. Vitusevich, M. Siegel, and N. Klein, *Phys. Rev. B* **72**, 064503 (2005).
27) V.P. Mineev, *Low Temp. Phys.* **37**, 1092 (2011).
28) C. Lu and S. Yip, *Phys. Rev.* B **78**, 132502 (2008).
29) Y. Tanaka, T. Yokoyama, A. V Balatsky, and N. Nagaosa, *Phys. Rev.* B **79**, 060505(R) (2009).
30) M. Sato and S. Fujimoto, *Phys. Rev. Lett.* **105**, 217001 (2010).

Received Nov. 13, 2018; Accepted Jan. 21, 2019

J. Magn. Soc. Jpn., **43**, 21-24 (2019)

<Paper>

Structure and magnetism of *c*-plane oriented $Mn_{50}(Te_{50-x}Sb_x)$ epitaxial thin films with NiAs-type structure

Y. Ashizawa*, S. Saito, M. Tsunoda, and M. Takahashi

Dept. of Electronic Engineering, Graduate School of Engineering, Tohoku University, *6-6-05, Aoba-yama, Sendai 980-8579*, Japan

*Present address: College of Science and Technology, Nihon University, *7-24-1 Narashinodai, Funabashi, Chiba 274-8501, Japan*

Structure, magnetism, and their correlation for NiAs-type $Mn_{50}(Te_{50-x}Sb_x)$ pseudo-single crystal films were investigated by changing the nearest Mn-Mn distance by substituting Te for Sb. The main results were as follows. First, *c*-plane oriented $Mn_{50}(Te_{50-x}Sb_x)$ pseudo-single crystal films were prepared in ranges of Sb composition, *x*, from 0 to 16 and from 33 to 51 by employing a *c*-plane oriented NiAs-type MnTe under-layer. Second, lattice parameter *a* of the $Mn_{50}(Te_{50-x}Sb_x)$ films was nearly constant at about 4.17 Å for $0 \le x \le 38$ and reduced gradually down to 4.13 Å for $x \ge 38$ as *x* increased. Lattice parameter *c* decreased with a gentle slope from 6.68 to 6.61 Å for $0 \le x \le 16$ and reduced gradually down to 5.78 Å for $x \ge 23$. As a result, $d_{Mn\text{-}Mn}$ changed from 3.34 Å to 2.89 Å. Third, the saturation magnetic moments m_S at 5 K linearly increased with a different slope as *x* increased for $0 \le x \le 11$ and $33 \le x \le 51$. Finally, the coefficient of $T^{3/2}$ in Bloch's law *A* decreased rapidly for $x \le 16$ as *x* increased, and it increased gradually for $16 \le x \le 51$ as *x* decreased.

Keywords: NiAs-type structure, Mn-Mn distance, Epitaxial growth, MnTe, MnSb

1. Introduction

The $Mn_{50}(Te_{50-x}Sb_x)$ ternary system with an NiAs-type hexagonal structure, which is a double hexagonal close-packed structure ordered with cation and anion atoms, is interesting in terms of the magnetism and structure of conductive Mn-compounds. NiAs-type MnSb with lattice parameters, a = 4.128 Å and c = 5.789 Å[1], is a ferromagnetic substance whose magnetic easy axes <11.0> lie in the *c*-plane[1-3] as shown in Fig. 1 (a), while NiAs-type MnTe is an antiferromagnetic substance whose spins align ferromagnetically and parallel to the *c*-plane in each atomic plane of Mn and are antiferromagnetically coupled with the adjacent atomic plane[4] as shown in Fig. 1 (b). The *a* of MnTe, which is equal to 4.142 Å, is very close to that of MnSb, and the *c* of MnTe, which is equal to 6.711 Å, is far from that of the MnSb[5,6]. Namely, the *c*-plane distance, corresponding to twice the nearest Mn-Mn distance, $d_{Mn\text{-}Mn}$, seems to decide the magnetism of NiAs-type Mn-compounds. It is thus expected to control the magnetism of these compounds by controlling the *c*-plane distance in the $Mn_{50}(Te_{50-x}Sb_x)$ ternary system.

In this study, we thus examined the structure, magnetism, and their correlation for NiAs-type $Mn_{50}(Te_{50-x}Sb_x)$ pseudo-single crystal films with Te substituted for Sb.

2. Experimental procedure

$Mn_{50}(Te_{50-x}Sb_x)$ pseudo-single crystal films with *c*-plane orientation were fabricated by using simultaneous DC sputtering with Mn, Te, and Sb targets on a Si(111) single crystal substrate. The sample compositions of the ternary $Mn_{50}(Te_{50-x}Sb_x)$ films are summarized in Table 1. The substrate was chemically cleaned and dry etched by Ar-ion bombardment before the film deposition. The thickness of the $Mn_{50}(Te_{50-x}Sb_x)$ films was constant at 100 nm. A B20-type MnSi epitaxial layer was used as a template for the epitaxial growth of the following MnTe under-layer and $Mn_{50}(Te_{50-x}Sb_x)$ films. The MnSi template layer was formed by a natural reaction

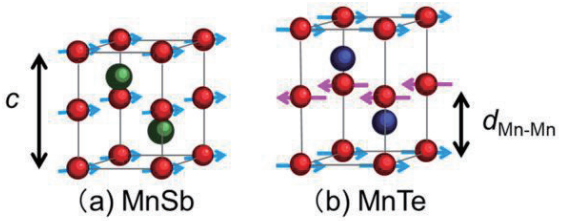

Fig. 1 Spin alignments of (a) NiAs-type MnSb, which is ferromagnetic substance, and (b) NiAs-type MnTe, which is antiferromagnetic substance.

Table 1 Compositions of *c*-plane oriented NiAs-type $Mn_{50}(Te_{50-x}Sb_x)$ pseudo-single crystal films fabricated by DC magnetron sputtering

Sample Composition *x*	C_{Mn} (at.%)	C_{Te} (at.%)	C_{Sb} (at.%)
0	50	50	0
5	49	46	5
11	48	41	11
16	51	33	16
23	50	27	23
29	50	21	29
33	50	17	33
38	49	13	38
50	49	1	50
51	49	0	51

between the Si substrate and a 1-nm-thick Mn layer with an elevated substrate temperature of 623 K[3,7]. As an under-layer, a *c*-plane oriented 50-nm-thick MnTe layer was formed on the MnSi template layer at 623 K by hetero-epitaxy. On the under-layer, the $Mn_{50}(Te_{50-x}Sb_x)$ films were grown epitaxially at 523–623 K with a deposition rate of about 0.1 nm/s.

The chemical composition of the ternary $Mn_{50}(Te_{50-x}Sb_x)$ films was determined in X-ray fluorescence analyses with Mn-*K*α, Sb-*L*α, and Te-*L*α lines. The crystal structures of the films were investigated by using two kinds of X-ray diffraction (XRD) methods; one was a conventional out-of-plane method of Bragg-Brentano geometry, and the other was an in-plane method of Gracing incidence geometry[8,9] with a Cu-*K*α line. The magnetic properties were measured by a vibrating sample magnetometer at room temperature (R.T.) and a superconducting quantum interference device magnetometer at various temperatures between 5 K and R.T.

3. Results

3.1 Structural properties of ternary $Mn_{50}(Te_{50-x}Sb_x)$ films

Fig. 2 shows XRD profiles of out-of-plane measurement for the ternary $Mn_{50}(Te_{50-x}Sb_x)$ films as a function of Sb composition, *x*. The diffraction lines observed at around $2\theta = 55°$ originated from the *c*-plane of the NiAs-type MnTe under-layers. For $0 < x \leq 16$, these diffraction lines had shoulders on the higher angle side, as indicated by the small arrows in Fig. 2. These shoulders were identified as the diffraction from the *c*-plane of the NiAs-type $Mn_{50}(Te_{50-x}Sb_x)$ layer, and the diffraction line shifted to a higher angle with the increase in Sb composition, *x*. For the sample of $x = 23$, another diffraction line suddenly appeared at around 62°. For $x \geq 23$, this diffraction line also shifted to a higher angle with the increase in *x* and finally reached the angle for the *c*-plane of the NiAs-type MnSb phase. Namely, the *c*-plane oriented NiAs-type $Mn_{50}(Te_{50-x}Sb_x)$ films with a gradual change in lattice constant, *c*, were fabricated in the respective composition ranges of $0 \leq x \leq 16$ and $23 \leq x \leq 51$. The $Mn_{50}(Te_{50-x}Sb_x)$ films with *c*-plane orientation were grown epitaxially, which was confirmed by using the in-plane XRD method.

Fig. 3 shows lattice parameters *a* and *c* and $d_{Mn\text{-}Mn}$ for the NiAs-type $Mn_{50}(Te_{50-x}Sb_x)$ films with *c*-plane orientation for $0 \leq x \leq 51$ as a function of *x*. Lattice parameters *a* and *c* were derived from the in-plane and out-of-plane XRD profiles, respectively. With the increase in *x*, *a* was almost constant at about 4.17 Å for $0 \leq x \leq 38$ and reduced down to 4.13 Å gradually for $x \geq 38$, whereas, with the increase in *x*, *c* slightly decreased from 6.68 to 6.61 Å for $0 \leq x \leq 16$, steeply dropped for $16 \leq x \leq 23$, and decreased gradually down to 5.78 Å for $x \geq 23$. As a result, $d_{Mn\text{-}Mn}$ changed from 3.34 to 2.89 Å in accordance with the change in *c*. The steep changes in *c* and $d_{Mn\text{-}Mn}$ from $x = 16$ to 23 imply that the NiAs-type $Mn_{50}(Te_{50-x}Sb_x)$ single phase for $16 \leq x \leq 23$ was not stable.

3.2 Magnetic properties of NiAs-type $Mn_{50}(Te_{50-x}Sb_x)$ pseudo-single crystal films

Fig. 4 shows saturation magnetic moments per Mn atom, m_S, for the NiAs-type $Mn_{50}(Te_{50-x}Sb_x)$ epitaxial films as a function of *x*. The m_S values were derived from the saturation magnetization of the films at 5 K. m_S can be observed even for $x = 5$. This shows that m_S was proportional to *x* with a gentle slope for $0 \leq x \leq 16$. With an increase in *x* from 33 to 51, m_S also showed a linear rise up to 3.23 μ_B/Mn, but the slope for $33 \leq x \leq 51$ was steeper than that for $0 \leq x \leq 16$.

To estimate the magnetic transition temperatures of the NiAs-type $Mn_{50}(Te_{50-x}Sb_x)$ epitaxial films, the coefficient of $T^{3/2}$, *A*, in Bloch's $T^{3/2}$ law was deduced in analyses of the temperature dependence of saturation

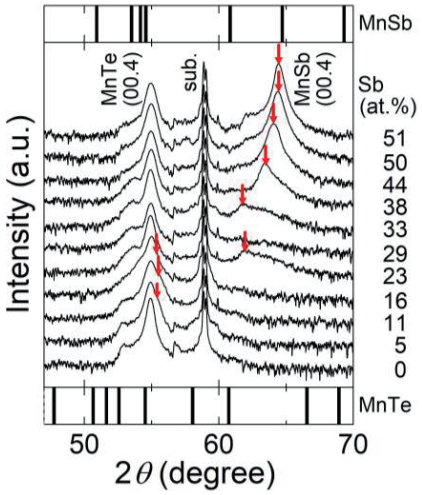

Fig. 2 Out-of-plane XRD profiles for ternary $Mn_{50}(Te_{50-x}Sb_x)$ films deposited on *c*-plane oriented MnTe epitaxial under-layer as function of Sb composition, *x*.

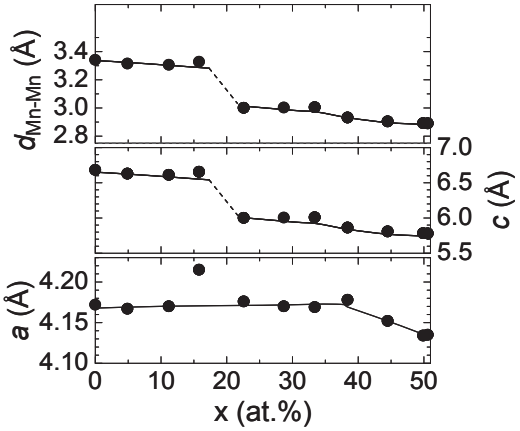

Fig. 3 Lattice parameters, *a* and *c*, and nearest Mn-Mn distance, $d_{Mn\text{-}Mn}$, for ternary NiAs-type $Mn_{50}(Te_{50-x}Sb_x)$ films as function of Sb composition, *x*.

magnetization at low temperature. Bloch's law[10] is as follows.

$$\frac{\Delta M(T)}{M(5K)} = A \cdot T^{3/2}, \quad (1)$$

$$A = C \cdot \left(\frac{k_B}{J}\right)^{3/2}, \quad (2)$$

where T is temperature, $\Delta M(T)$ is the difference in saturation magnetization at T, $M(T)$, and at 5 K, M(5K), k_B is Boltzmann's constant, J is an exchange integral, and C is a coefficient. The change in A as a function of x is shown in Fig. 5. A decreased rapidly for $x \leq 16$ and slightly for $16 \leq x \leq 51$ with the increase in x.

The transition temperatures were estimated from Bloch's $T^{3/2}$ law and mean field approximation,

$$T^{cal.} = \frac{2zJS(S+1)}{3k_B}, \quad (3)$$

where z is the number of nearest neighbors, and S is the spin of Mn. The Curie temperatures, $T_C^{cal.}$s, of the $Mn_{50}(Te_{50-x}Sb_x)$ epitaxial films for $5 \leq x \leq 51$ were estimated by substituting the J value from Eq. 2 into Eq. 3 and were plotted with filled circles in Fig. 6 as a function of the Mn-Mn distance obtained for Fig. 3. The estimated $T_C^{cal.}$s were normalized by the Curie temperature of bulk MnSb at 586 K[1,11]. The Néel temperature T_N of bulk MnTe at 307 K is also plotted in Fig. 6. With the increase in $d_{Mn\text{-}Mn}$, $T_C^{cal.}$ reduced monotonically for 2.89 Å $\leq d_{Mn\text{-}Mn} \leq$ 3.01 Å and increased monotonically for 3.31 Å $\leq d_{Mn\text{-}Mn} \leq$ 3.34 Å.

4. Discussion

In both of the compositional dependences of m_S and A, a discontinuous change existed at the same compositional region, $16 \leq x \leq 23$. This suggests that the magnetism of the NiAs-type $Mn_{50}(Te_{50-x}Sb_x)$ films for $0 \leq x \leq 11$ was different from that for $33 \leq x \leq 51$. The decrease in m_S for $33 \leq x \leq 51$ with the reduction in x may be explained as follows. The ferromagnetically aligned local magnetic moments of the Mn atoms were reduced by the increase in the amount of substituted Te atoms. From the results of Fig. 4, the slope of m_S for $33 \leq x \leq 51$ can be formularized as:

$$m_S = 3.23 \cdot (x / 50). \quad (4)$$

Here, 3.23 means the magnetic moment per Mn atom in MnSb. The reducing tendency of m_S is also shown by the broken line in Fig. 4. For $33 \leq x \leq 51$, the broken line, which passes through the origin, is in good agreement with the experimental trend.

The appearance and increase in m_S for $0 \leq x \leq 11$ with the rise in x may be explained as follows. The antiferromagnetic coupling between the adjacent Mn-atomic layers still existed up to $x = 11$; as a result, ferrimagnetism appeared, and the difference in sub-lattice moments increased as x increased. In this case, the slope for m_S is:

$$m_S = (5.0–3.23) \cdot (x / 50) = 1.77 \cdot (x / 50). \quad (5)$$

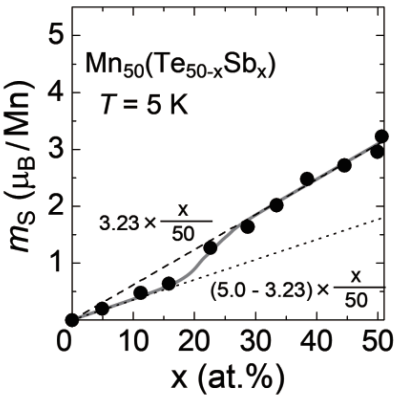

Fig. 4 Change in saturation magnetic moments per Mn atom, m_S, for $Mn_{50}(Te_{50-x}Sb_x)$ epitaxial films as function of Sb composition, x. m_S were derived from saturation magnetization of film at 5 K.

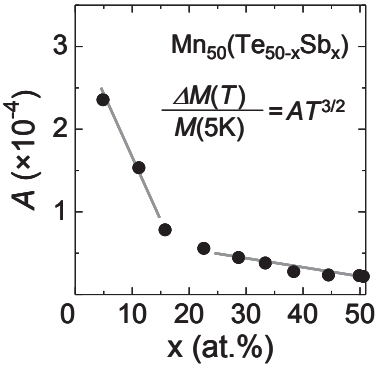

Fig. 5 Change in A, which is coefficient of $T^{3/2}$ in Bloch's law, for $Mn_{50}(Te_{50-x}Sb_x)$ epitaxial films as function of Sb composition, x.

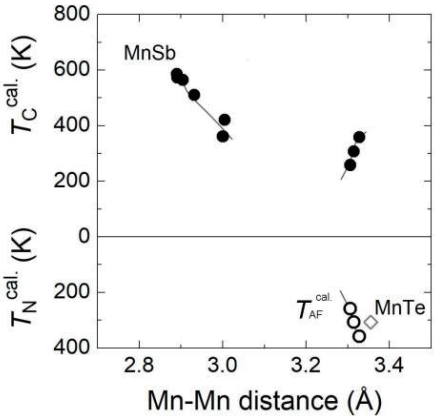

Fig. 6 Change in estimated Curie temperature, $T_C^{cal.}$, and estimated Néel temperature, $T_N^{cal.}$, of $Mn_{50}(Te_{50-x}Sb_x)$ epitaxial films as function of nearest Mn-Mn distance, $d_{Mn\text{-}Mn}$. Magnetic transition temperatures were estimated from mean field approximation and Bloch's $T^{3/2}$ law in analyses of temperature dependence of saturation magnetization at low temperature.

Here, 5.0 and 3.23 mean the magnetic moment per Mn atom in MnTe and MnSb, respectively. 1.77 means the difference of it between MnTe and MnSb. The increasing tendency of m_S is shown by the dotted line in Fig. 4. For $0 \leq x \leq 11$, the dotted line, which starts from the origin, also corresponded to the experimental trend.

It is thought that the NiAs-type $Mn_{50}(Te_{50-x}Sb_x)$ system has ferromagnetic coupling in a short Mn-Mn distance, $d_{Mn\text{-}Mn} \leq 3.01$ Å, and has antiferromagnetic coupling in a long Mn-Mn distance, $d_{Mn\text{-}Mn} \geq 3.31$ Å as shown in Fig. 5. Therefore, if $T_{AF}^{cal.}$ is defined as the transition temperature at which the antiferromagnetic coupling of spins is destroyed by thermal energy, $T_C^{cal.}$ for $d_{Mn\text{-}Mn} \geq 3.31$ Å can be equal to $T_{AF}^{cal.}$. $T_{AF}^{cal.}$s are plotted with open circles on the $T_N^{cal.}$ side in Fig. 6. $T_{AF}^{cal.}$ shows good continuity from binary MnTe to ternary $Mn_{50}(Te_{50-x}Sb_x)$ in the region.

M-H curves of the $Mn_{50}(Te_{50-x}Sb_x)$ epitaxial films were measured at 5 K to clarify the difference in magnetism for each compositional region. The *M-H* curves of the films for x = 11, 16, and 33 are shown in Fig. 7. The cases of x = 11 and 33 represent the cases of ferrimagnetism and ferromagnetism, respectively. In both cases, the curves showed typical hysteresis loops of a magnetically single phase. In the case of x = 16, the transition region, the *M-H* curve shows steps around H = ±1 kOe. These steps indicated multiple magnetic phases in the film. This means that the ferrimagnetism and ferromagnetism co-existed in the transition region, $16 \leq x \leq 23$.

According to these explanations, we may say that the magnetism for $16 \leq x \leq 23$ cannot be connected smoothly with that for $0 \leq x \leq 11$ and $x \geq 33$, in particular, the sign of inter-atomic-layer exchange coupling. This suggests that the structural instability of NiAs-type $Mn_{50}(Te_{50-x}Sb_x)$ epitaxial films is possibly induced by the discontinuity of their magnetism in the transition region.

5. Conclusion

Structure, magnetism, and their correlation for NiAs-type $Mn_{50}(Te_{50-x}Sb_x)$ pseudo-single crystal films were investigated by changing the nearest Mn-Mn distance by substituting Te for Sb.

The *c*-plane oriented $Mn_{50}(Te_{50-x}Sb_x)$ pseudo-single crystal films were prepared in ranges of Sb composition, x, from 0 to 16 and from 33 to 51 by employing a *c*-plane oriented NiAs-type MnTe under-layer.

Lattice parameter a of the $Mn_{50}(Te_{50-x}Sb_x)$ films changed from 4.17 to 4.13 Å, and c changed from 6.68 to 5.78 Å, As result, the nearest Mn-Mn distance, $d_{Mn\text{-}Mn}$, changed from 3.34 to 2.89 Å.

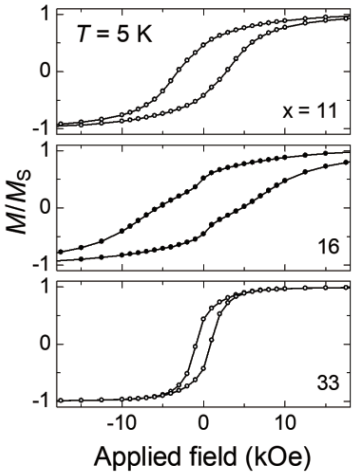

Fig. 7 *M-H* curves of $Mn_{50}(Te_{50-x}Sb_x)$ (x = 11, 16, and 33) epitaxial films measured at 5 K.

The saturation magnetic moments m_S of Mn atoms at 5 K linearly increased with a different slope as x increased, $0 \leq x \leq 11$ and $33 \leq x \leq 51$.

The coefficient of $T^{3/2}$ in Bloch's law, A, decreased rapidly for $x \leq 16$ as x increased and increased gradually for $16 \leq x \leq 51$ as x decreased.

The magnetism of the ternary NiAs-type $Mn_{50}(Te_{50-x}Sb_x)$ system changed smoothly from antiferromagnetism to ferrimagnetism and discontinuously from ferrimagnetism to ferromagnetism by decreasing $d_{Mn\text{-}Mn}$.

References

1) T. Okita and Y. Makino: *J. Phys. Soc. Jpn.*, **25**, 120 (1968).
2) Y. Ashizawa, S. Saito, and M. Takahashi: *J. Appl. Phys.*, **91**, 8240 (2002).
3) S. Saito, Y. Ashizawa, H. Shoji, and M. Takahashi: *J. Magn. Soc. Jpn.*, **25**, 855 (2001) [in Japanese].
4) N. Kunitomi, Y. Hamaguchi, and S. Anzai: *J. Phys.*, **25**, 568 (1964).
5) I. Oftedal: *Z. Phys. Chem.*, **128**, 135 (1927) [in German].
6) S. Greenwald: *Acta Crystallogr.*, **6**, 396 (1953).
7) Y. Ashizawa, S. Saito, and M. Takahashi: *J. Appl. Phys.*, **91**, 8096 (2002).
8) W. C. Marra, P. Eisenberger, and A. Y. Cho: *J. Appl. Phys.*, **50**, 6927 (1979).
9) K. Omote and S. Y. Matsuno: *Adv. X-ray Chem. Anal.*, **30**, 205, (1998) [in Japanese].
10) F. Bloch: *Z. Physik.*, **61**, 206 (1930).
11) H. Ido: *J. Phys. Soc. Jpn.*, **25**, 625 (1968).

Received August 02, 2018; Accepted December 25, 2018

J. Magn. Soc. Jpn., **43**, 25-28 (2019)

<Paper>

Near-Infrared Magneto-Refractive Effect for Antiferro-Magnetically Exchange Coupled Co/Ru Multilayer Film in Transmission Configuration

S. Saito, H. Sato, K. Ooki, K. Akahane, and H. Uchida*

Department of Electronic Engineering, Graduate School of Engineering, Tohoku Univ., *6-6-05, Aoba, Aramaki, Aoba-ku, Sendai, Miyagi, 980-8579 Japan*

* Electrical and Electronic Information Engineering, Toyohashi Univ. of Technology, *1-1, Hibarigaoka, Tempaku, Toyohashi, Aichi, 441-8580 Japan*

A magneto-refractive effect in a near-infrared (IR) region was investigated with a transmission configuration (T-MRE) for antiferro-magnetically coupled Co/Ru multilayer films. Applying dielectric function analysis based on an expanded Drude model that takes spin-dependent scattering into account, it was found that (1) a [Co(4 nm)/ Ru(0.7 nm)]$_{10}$ multilayer film took parallel to antiparallel magnetization states at H = 14 kOe to 0 Oe, respectively, and (2) that T-MRE curves against H took the maximum in the near-IR region and the minimum in the middle wavelength IR region. (3) The magnitude and wavelength dependence of T-MRE were well fitted by using the expanded Drude model with $\omega_p = 1.5 \times 10^{16}$, $\tau_{SAL} = 0.66$, and $\beta_{SAL} = 0.125$, where τ_{SAL} and β_{SAL} were self-averaged relaxation time and spin asymmetry, and ω_p was the plasma angular frequency of conduction electrons. (4) According to calculation based on the expanded Drude model, the T-MRE of $\Delta T/T$ showed the maximum of 0.3% at around 700 nm, and in the longer wavelength region, it showed a saturated feature with a value of –1.3% at around 3 μm.

Key words: magneto-refractive effect, spin-dependent scattering, expanded Drude model, dielectric constant spectrum

1. Introduction

Much attention has been paid to magnetic sensors with an optical probe (MSOP), since the sensor head can be relatively miniaturized and used under vacuum, liquid atmospheres through narrow space with an optical fiber. In order to realize MSOP with a simple optical system, an effect with light intensity change is more promising than that with light polarization change. Therefore, development of materials whose optical properties such as reflectivity and transmittance vary against magnetic field (H) is eagerly required. Based on this point, we focused on magneto-refractive effect (MRE) for antiferro-magnetically coupled ferro-/ non-ferromagnetic multilayer films where we can expect linear response against H with rotational magnetization process. Concerning MRE, theoretical studies were reported after 1995 [1], and experimental researches after 2002 [2]. According to these papers and following reports[3-6], the main interest is how to measure giant magnetoresistance (GMR) effect with contactless probe especially for Co-Ag related granular or Co/Cu related multilayer films, because the origin of both MRE and GMR is generally understood to be the spin-dependent scattering of conduction electrons. However, optical properties and transport properties are not completely the same; concerning the MRE with transmission configuration (T-MRE), there exists wavelength dependence, and it is desirable that total thickness of a multilayer film should be thin to obtain enough transmitted light intensity for detection, which is completely different situation for GMR. In this sense, material investigations of MRE itself have not sufficiently carried out. Therefore, in this study, we experimentally obtained MRE with the transmission configuration for Co/Ru multilayer films with RKKY-like interlayer exchange coupling[7–8] as a typical multilayer system. Furthermore, we applied dielectric function analysis, and discussed material guide for enhancing T-MRE based on an expanded Drude model taking the spin-dependent scattering into account.

2. Experimental procedure

The multilayer films were fabricated by dc magnetron sputtering on glass substrates. A Ti(2 nm)/ Ru(3 nm) layer was adopted as an underlayer for the purpose of adhesion of the film to the substrate and the control of crystalline sheet texture with atomic closed packed plane parallel to the film plane. A SiN with 10 nm thick was used as a capping layer to avoid oxidation. The stacking structure of the magnetic multilayer was [Co(4 nm)/ Ru(d_{Ru} nm)]$_N$ with the repetition number N of 10 with changing d_{Ru} from 0 to 1.2 nm. Here, Ru was selected as a nonmagnetic layer material to stabilize antiparallel magnetical coupling state under zero field with a thinner film thickness than that of Cu by RKKY-like interlayer exchange coupling.

Magnetic properties were evaluated by the vibrating sample magnetometer with the maximum applied field (H_{max}) of 14 kOe. Optical properties were

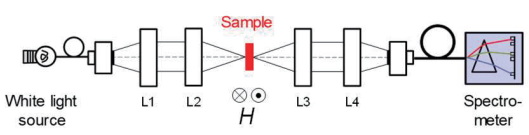

Fig. 1 Schematic of system for measuring spectroscopic magneto-refractive effect with transmission configuration. L1 to L4 are condensing and collimation lens.

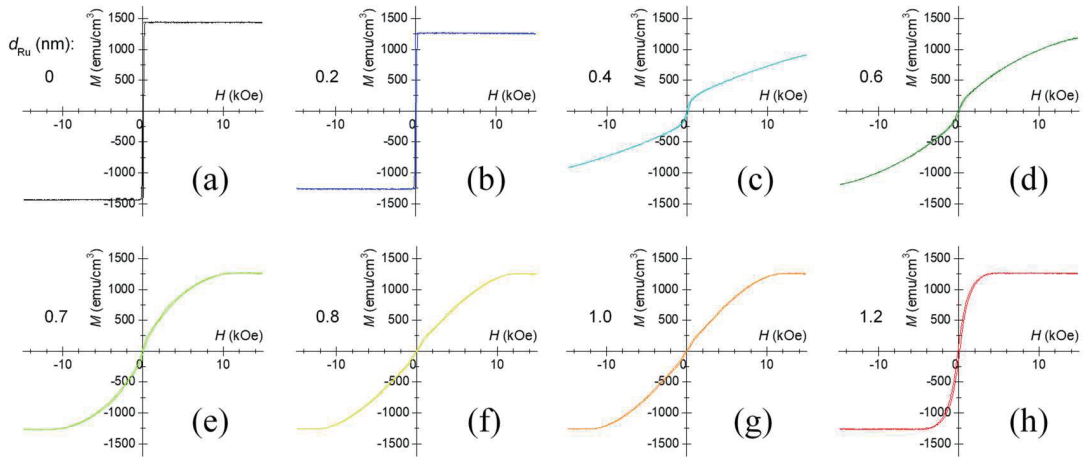

Fig. 2 Magnetic hysteresis loops for [Co(4 nm)/Ru(d_{Ru} nm)]$_{10}$ multilayer films with d_{Ru} of (a) 0, (b) 0.2, (c) 0.4, (d) 0.6, (e) 0.7, (f) 0.8, (g) 1.0, and (h) 1.2 nm.

spectroscopically measured by the ellipsometer (M-2000, J. A. Woollam) with the wavelength region from 250 to 1700 nm. T-MRE was spectrometrically measured by a hand-made system with an electromagnet applying magnetic field (H) along the film plane direction[9] as shown in Fig. 1. Here, the measurement wavelength (λ) range was 900–1650 nm limited by monochrometer (NIR-QUEST, Ocean Optics) and H_{max} was 14 kOe.

3. Results and discussion

3.1 Magnetic properties

Figure 2 shows typical magnetic hysteresis loops with the Co/Ru multilayer films with the Ru thickness, d_{Ru} of (a) 0, (b) 0.2, (c) 0.4, (d) 0.6, (e) 0.7, (f) 0.8, (g) 1.0, and (h) 1.2 nm, respectively. In the loops of (a) and (b), steep magnetization process can be seen around $H = 0$ caused by magnetic domain wall motion with ferromagnetically interlayer coupling between Co layers. With increasing d_{Ru}, saturation field becomes beyond 14 kOe, due to the antiferro-magnetic interlayer coupling, while the wall motion magnetization process remains for the films with (c) and (d). Further increasing d_{Ru} at (e) to (h), wall motion process completely disappears and smooth rotational magnetization process with the scissors type is expected.

3.2 Optical properties and magneto-refractive effect

Transmittance (T) of the [Co(4 nm)/ Ru(0–1.2 nm)]$_{10}$ multilayer films was measured and was found to be the magnitude of 0.5 to 1.7 % in the spectral range of 900–1650 nm (data not shown). In details, T monotonously increases with increasing λ, and T monotonously decreases with thickening d_{Ru}.

Figure 3 shows hysteresis curves in transmittance normalized by that of under 14 kOe of λ at 1550 nm against H for typical samples with [Co(4 nm)/ Ru(0, 0.4, 0.7 nm)]$_{10}$, whose magnetic properties are shown in Fig. 2 (a), (c) and (e), respectively. Here, T-MRE was defined as difference in transmittance between that of under H = 14 kOe and 0 kOe normalized by that of under 14 kOe. As seen in Fig. 3 (a), no change in T against H was observed even though the sample shows magnetization process with ferromagnetic hysteresis shown in Fig. 2 (a). On the other hand, as seen in Fig. 3 (c) and (e), T changed symmetrically with the H = 0 axis. Compared with the transmittance hysteresis curves of (c) and (e), saturation feature under high H region cannot be observed in (c) but clearly observed in (e). These facts mean that the shape of transmittance curves of the present multilayer films reflects angles between magnetic moments of neighboring layers such as GMR effect rather than direction of magnetic moments as shown in Fig. 2.

Figure 4 shows the normalized transmittance map with [Co(4 nm)/ Ru(0, 0.4, 0.7)]$_{10}$ multilayer films (color

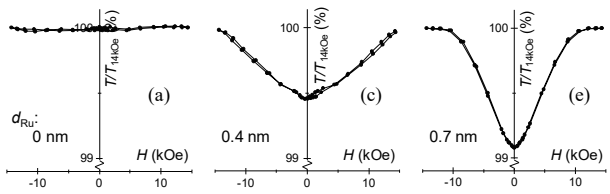

Fig. 3 MRE curves of wavelength at 1550 nm with thru beam configuration for [Co(4 nm)/Ru(d_{Ru} nm)]$_{10}$ multilayer films with d_{Ru} of (a) 0, (c) 0.4, and (e) 0.7 nm.

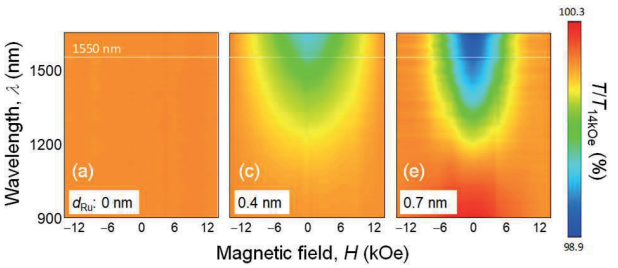

Fig. 4 Color maps of MRE with transmittance configuration plotted against wavelength and applied magnetic field for [Co(4 nm)/Ru(d_{Ru} nm)]$_{10}$ multilayer films with d_{Ru} of (a) 0, (c) 0.4, and (e) 0.7 nm. White lines with wavelength of 1550 nm correspond to curves shown in Fig. 3.

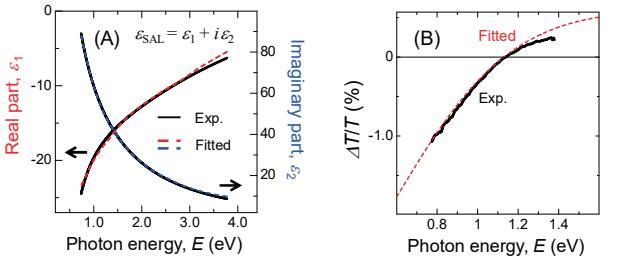

Fig. 5 (A) Dielectric constants and (B) T-MRE spectrum for [Co(4 nm)/Ru(0.7 nm)]$_{10}$ multilayer film. Black solid lines mean experimental results, and blue and red broken lines are results fitted by using oscillation model with expansion Drude term.

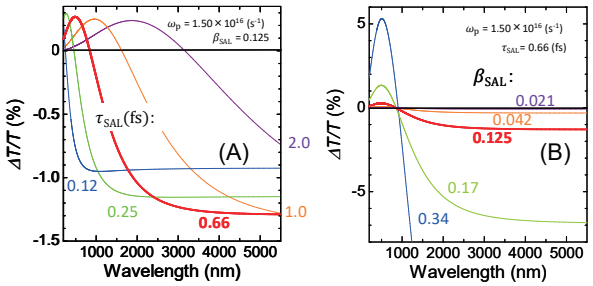

Fig. 6 T-MRE spectra calculated by changing (A) t_{SAL} and (B) b_{SAL} for [Co(4 nm)/Ru(0.7 nm)]$_{10}$ multilayer film. In calculation, constant values of $w_p = 1.5\times10^{16}$ and $b_{SAL} = 0.125$ for (A) and $w_p = 1.5\times10^{16}$ and $t_{SAL} = 0.66$ for (B) were used.

on line). The vertical and horizontal axes indicate λ and H. The white lines with λ = 1550 nm correspond to the curves shown in Fig. 3 (a), (c) and (e). As seen in Fig. 4 (a), no change can be seen, whereas in (b) and (c), the minimum and the maximum appears around H = 0. Focusing on λ dependence of the sample (e), the minimum can be observed at λ = 900 nm. With increasing λ up to 1100 nm, the magnitude of the minimum decreases. Further increasing of λ over 1100 nm, this minimum changes into the maximum. The magnitude of the maximum enhances with increasing λ in the present experimental range. In the following section, we select the sample (e), because we can realize parallel (H = 14 kOe) and antiparallel (H = 0 kOe) magnetization states in our experimental setup of T-MRE.

3.3 Dielectric function analysis with expanded Drude model

In order to understand the enhancement phenomenon and change in the extreme values from the maximum to the minimum in wavelength dependence of T-MRE, we carried out spectral analysis for dielectric function. According to M. Vopsaroiu et al.[4] dielectric function for a GMR multilayer film (self-averaging limit of dielectric constant ε_{SAL}), assuming the multilayer to be a single layer, is written by following formula;

$$\varepsilon_{SAL} = 1 - \frac{{\omega_p}^2}{\omega^2}\frac{-i\omega\tau_{SAL}}{1-i\omega\tau_{SAL}}\left(1 - \frac{{\beta_{SAL}}^2\left(\frac{M}{M_s}\right)^2}{\left(1-i\omega\tau_{SAL}\right)^2 - {\beta_{SAL}}^2\left(\frac{M}{M_s}\right)^2}\right), \quad (1)$$

where τ_{SAL} and β_{SAL} are self-averaged relaxation time and spin asymmetry, ω_p is the plasma angular frequency of conduction electrons, ω is the angular frequency of the incident light. M/M_s is the normalized magnetization and takes 1 for the parallel state (saturation) and 0 for the antiparallel state. In the eq. (1), the first term is the so-called Drude term and second one is an expansion Drude term taking spin-dependent scattering into consideration. Here, eq. (1) is based on the form of complex refractive index of $N = n + i\kappa$. By applying this equation, we can derive τ_{SAL} and β_{SAL} from fitting analysis to optical and T-MRE spectra obtained by the experiment.

Figure 5 shows (A) Dielectric constants and (B) T-MRE spectrum for the [Co(4 nm)/Ru(0.7 nm)]$_{10}$ multilayer film. Black solid lines mean experimental results, and broken lines with blue and red color are fitted results by using an oscillation model with the expansion Drude term. According to the ellipsometry, application of the oscillation model in fitting shown in Fig. 4 (A) revealed $\omega_p = 1.5 \times 10^{16}$ and τ_{SAL} = 0.66. Next, T-MRE spectrum was fitted based on eq. (1) shown in Fig. 5 (B) through calculations of transmittance of parallel and antiparallel states, which resulted in β_{SAL} = 0.125.

Finally, we expected material guide to enhance T-MRE by calculation to expand spectral range. Figure 6 shows calculated T-MRE spectra for virtual multilayer films by changing (A) τ_{SAL} around 0.66 and (B) β_{SAL} around 0.125. In the calculation, constant values of $\omega_p = 1.5 \times 10^{16}$ and β_{SAL} = 0.125 for (A) and $\omega_p = 1.5 \times 10^{16}$ and τ_{SAL} = 0.66 for (B) are used. Here, $\omega_p = 1.5 \times 10^{16}$, τ_{SAL} = 0.66 and β_{SAL} = 0.125 are the values obtained by fitted results as shown in Fig. 5. For all conditions, the sign of T-MRE of $\Delta T/T$ changes positive to negative with increasing λ. As seen in (A) for the condition of τ_{SAL} = 0.66 which corresponds to the present [Co(4 nm)/Ru(0.7 nm)]$_{10}$ multilayer film, $\Delta T/T$ shows the maximum of 0.3% at around 700 nm, whereas in the longer wavelength region, it shows the saturated feature to the value of –1.3% at around 3 μm. Therefore, the effect of the enhancement of the magnitude of T-MRE in Mid-wavelength IR region (negative sign) was found to be larger than that in Near IR region (positive sign). With increasing τ_{SAL}, λ where the sign of $\Delta T/T$ changes from the positive to the negative shifts toward the longer λ side as shown in (A). In contrast, with increasing β_{SAL}, degree of enhancement increases as shown in (B). Therefore, considering of application of MRE, figure of merit can be increased by ferro-/ nonferro-magnetic material combination, layer structure, and total thickness while realizing antiparallel magnetization states for thinner crystalline ferro-/ non-ferromagnetic multilayers.

4. Conclusion

A magneto-refractive effect in a near-infrared (IR) region was investigated with a transmission configuration (T-MRE) for Co/Ru multilayer films. As results, It was found that (1) a [Co(4 nm)/ Ru(0.7 nm)]$_{10}$

multilayer film with antiferro-magnetically coupling showed the magnitude of T-MRE of about −1% at 1550 nm, (2) the magnitude and wavelength dependence of T-MRE were well fitted by an expanded Drude model with $\omega_p = 1.5\times10^{16}$, $\tau_{SAL} = 0.66$ and $\beta_{SAL} = 0.125$, where τ_{SAL} and β_{SAL} were self-averaged relaxation time and spin asymmetry, ω_p was the plasma angular frequency of conduction electrons, and (3) according to calculation based on the expanded Drude model, the T-MRE of $\Delta T/T$ showed a saturated feature with a value of −1.3% at around 3 μm. Further increase of $\Delta T/T$ in IR region is expected to enhance β_{SAL} of the multilayer.

References

1) J. C. Jacquet and T. Valet, *Mater. Res. Soc.*, **384**, 477 (2015).
2) V. G. Kravets, D. Bozec, J.A. Matthew, S. M. Thompson, H. Menard, A. B. Horn, and A. F. Kravets, *Phys. Rev. B*, **65**, 054415 (2002).
3) A. B. Granovskii, M. V. Kuz'michev, and J. P. Clerc, *J. Exp. Theor. Phys.*, **89**, 955 (1999).
4) M. Vopsaroiu, J. A. D. Matthew, and S. M. Thompson, *Rev. Sci. Instrum.*, **75**, 3127 (2004).
5) Jian-Qing Wang, Malak T.Sidney, Jared D. Rokitowski, Nam H. Kim, and Keqiang Wang, *J. Appl. Phys.*, **103**, 07F316 (2008).
6) M. Vopsaroiu, M. G. Cain, and V. Kuncser, *J. Appl. Phys.*, **110**, 056103 (2011).
7) S.S.P. Parkin, N. More, and K.P. Roche, *Phys. Rev. Lett.*, **64**, 2304 (1990).
8) P.J.H. Bloemen, H.W. van Kesteren, H.J.M. Swagten, and W.J.M. de Jonge, *Phys. Rev. B*, **50**, 13505 (1994).
9) Haruhiko Sato, Shin Saito, Shyota Mizuno, Koichi Akahane and Hironaga Uchida, *IEEJ Trans. Fund. Mater.*, **136**, 174 (2016).

Received Oct. 15, 2018; Accepted Jan. 17, 2019

J. Magn. Soc. Jpn., **43**, 29-33 (2019)

<Paper>

Anomalous Hall Effect and Anisotropic Magnetoresistance in Perpendicularly Magnetized $FePt_{1-x}Pd_x$ Films

T. Seki[*,**] , S. Kikushima[*], and K. Takanashi[*,**]

[*]Institute for Materials Research, Tohoku University, *Sendai 980-8577, Japan*

[**]Center for Spintronics Research Network, Tohoku University, *Sendai 980-8577, Japan*

$L1_0$-ordered alloys with high uniaxial magnetic anisotropy (K_u) are key materials for future spintronic devices to realize large-scale integration. In this study, we investigated the anomalous Hall effect (AHE) and anisotropic magnetoresistance (AMR) effect for $FePt_{1-x}Pd_x$ (001) epitaxial films. Highly $L1_0$-ordered structures and perpendicular magnetization were obtained for all the compositions. The FePt film exhibited the highest K_u and the largest anomalous Hall angle (θ_{AHE}) among the present $FePt_{1-x}Pd_x$ samples, and the values of K_u and θ_{AHE} were gradually decreased as the Pd concentration increased. In addition, the composition dependence of the AMR ratio showed a similar tendency to those for K_u and AHE. We discuss possible scenarios to explain these composition dependencies.

Key words: $L1_0$-type ordered alloy, anomalous Hall effect, anisotropic magnetoresistance effect

1. Introduction

For the further progress in magnetic storage technology, we need to tackle several essential problems every magnetic material has. One of the inevitable problems is the thermal instability of magnetization appearing as the volume of magnet (V) is reduced. In order to hurdle this problem, high uniaxial magnetic anisotropy (K_u) is needed because the thermal stability factor (Δ) of magnetization is given by $\Delta = K_u V / k_B T$, where k_B is the Boltzmann constant and T is the temperature. Thus, high K_u materials are key to maintain sufficient Δ even for a nanometer-scaled magnet, enabling us to realize the large-scale integration of spintronic devices.

$L1_0$-ordered alloys are representative high K_u materials[1]. Thanks to their high K_u along the c-axis of $L1_0$-ordered structure, perpendicularly magnetized layers can be formed when those alloys are grown with the (001) crystal orientation in the thin film form[2-5]. This characteristic is beneficial for perpendicular magnetic recording and spintronic devices utilizing perpendicular magnetization as a perpendicular spin-polarizer[6]. Among the $L1_0$-ordered alloys, $L1_0$-FePt and $L1_0$-FePd are famous alloys, and are regarded as candidate materials for ultrahigh density magnetic storage. Although both alloys have similar characteristics, such as high K_u values and structures being composed of Fe and Pt or Pd with large spin-orbit interaction, there are also definite differences between them. The most intriguing difference is the magnitude of magnetization damping. $L1_0$-FePd exhibits a much smaller damping constant than that of $L1_0$-FePt[7,8]. Although that might be partially interpreted by the smaller spin orbit interaction of Pd than that of Pt, the relationship between the transport properties and the spin orbit interaction has not been totally understood yet for the Fe-Pt-Pd system [9-12].

In this study, we focus on the anomalous Hall effect (AHE) and anisotropic magnetoresistance (AMR) effect. The magnitude of AHE is characterized by the anomalous Hall angle (θ_{AHE}). The spin-orbit interaction is regarded as an essential factor for AHE, and several mechanisms, such as skew scattering, side jump and intrinsic deflection, are responsible for the appearance of AHE[13]. The expression of AMR also includes the spin-orbit coupling constant[14]. Namely, both AHE and AMR are phenomena related with the spin-orbit interaction although they are often discussed in the different theoretical frameworks.

We prepared $FePt_{1-x}Pd_x$ (001) epitaxial films and systematically investigated the structures, magnetic properties and transport properties. The Pd concentration (x) dependences of K_u, AHE and AMR are compared, and possible scenarios to understand those composition dependences are qualitatively discussed.

2. Experimental Procedure

50 nm-thick $FePt_{1-x}Pd_x$ layers were directly grown on an MgO (001) single crystal substrate by employing the ultrahigh vacuum compatible magnetron sputtering apparatus. The base pressure of main growth chamber was below 2×10^{-7} Pa. The main growth chamber was equipped with three independent sputtering cathodes, where Fe, Pt, and Pd targets were installed. This cathode arrangement enabled us to vary the alloy composition by tuning the input powers for sputtering cathodes. The growth temperature for the $FePt_{1-x}Pd_x$ layers was set at 500°C. This high temperature process is indispensable to promote the $L1_0$-ordering. We monitored the film growth by employing reflection high-energy electron diffraction, which exhibited streak patterns for all the samples. This indicated that flat surfaces were obtained. The thin films were patterned into a Hall cross shape in order to measure AHE and AMR through the use of photolithography and Ar ion milling. The width of Hall cross was designed to be 20

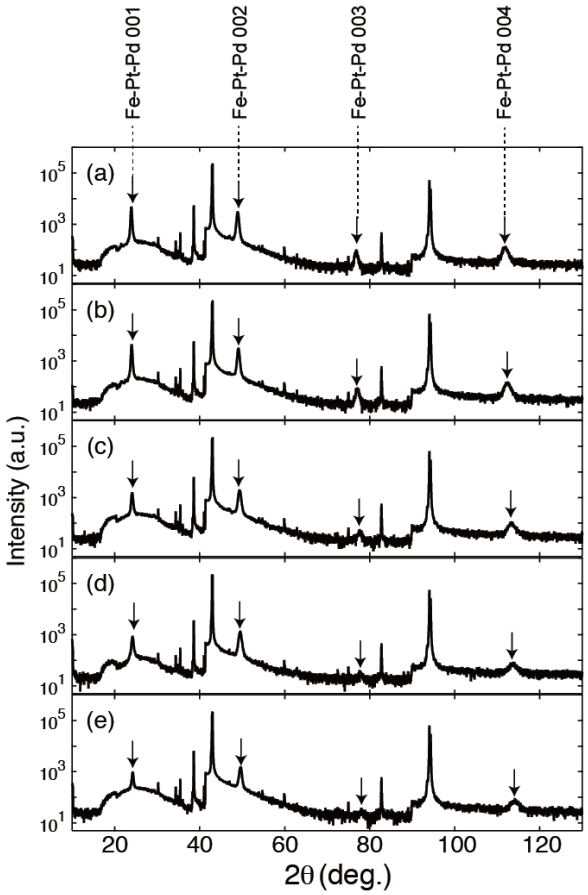

Fig. 1 Out-of-plane x-ray diffraction profiles for $FePt_{1-x}Pd_x$ films with (a) x = 0, (b) 0.25, (c) 0.5, (d) 0.75, and (e) 1.

μm.

The structure was characterized using the x-ray diffraction (XRD) with Cu-$K\alpha$ radiation. Magnetization measurements were carried out at room temperature using a superconducting quantum interference device magnetometer. Transport properties were measured at room temperature using a physical property measurement system (PPMS) with the maximum magnetic field of 90 kOe.

In this study, we set the Pd concentration x in $Pt_{1-x}Pd_x$ at 0, 0.25, 0.5, 0.75, and 1, where $x \times 100$ corresponds to the atomic percent of Pd concentration. The actual alloy compositions were determined to be $Fe_{48}Pt_{52}$ (for x = 0), $Fe_{48}Pt_{45}Pd_7$ (for x = 0.25), $Fe_{53}Pt_{22}Pd_{25}$ (for x = 0.5), $Fe_{48}Pt_8Pd_{44}$ (for x = 0.75), and $Fe_{51}Pd_{49}$ (for x = 1) by electron probe x-ray microanalysis. Hereafter, the designed Pd concentration x refers to the sample name instead the measured composition for simplicity.

3. Results and Discussion

First, we explain the structure and the magnetic properties for the $FePt_{1-x}Pd_x$ films. Figure 1 shows the XRD profiles for (a) x = 0, (b) 0.25, (c) 0.5, (d) 0.75, and (e) 1. The unlabeled sharp peaks come from the reflections of the MgO substrate. All the peaks, denoted by the arrows, are 00l reflections of $FePt_{1-x}Pd_x$, which indicates that all the $FePt_{1-x}Pd_x$ layers show the (001) epitaxial growth on the MgO (001) substrate. In addition to the 002 and 004 fundamental peaks, the 001 and 003 superlattice peaks are clearly observed, suggesting the formation of $L1_0$-ordered structure.

The lattice constants of c-axis and a-axis, tetragonality (c/a), and the degree of long-range order (S) are summarized in Figs. 2 (a), (b), (c) and (d), respectively. The lattice constants of c-axis were obtained from the (002) peaks in the out-of-plane XRD profile (Fig. 1) whereas those of a-axis were obtained from the 200 peaks in the in-plane XRD profiles (not shown here). S is defined as[2,3]

$$S^2 = \frac{\left[I_{\mathrm{super}}/I_{\mathrm{fund}}\right]_{\mathrm{obs}}}{\left[I_{\mathrm{super}}/I_{\mathrm{fund}}\right]_{\mathrm{calc}}^{S=1}}, \quad (1)$$

where I_{fund} and I_{super} are the integrated intensities of fundamental and superlattice peaks, respectively, and the subscripts of obs and calc represent the experimentally observed values and the calculated values, respectively. The intensities for the fully ordered state (S = 1) were calculated with taking into account atomic scattering factors, Debye-Waller factors, Lorentz factor, polarization factor, and structure factors[2,3]. In

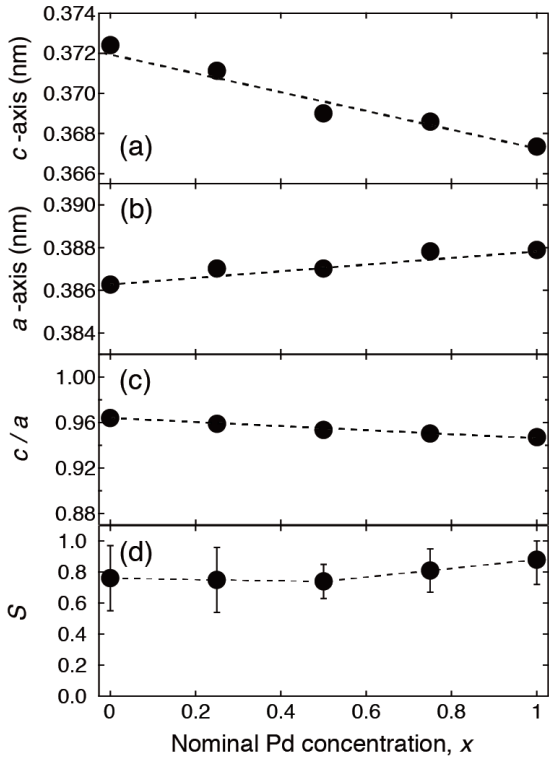

Fig. 2 Lattice constants of c-axis and a-axis, tetragonality (c/a), and the degree of long-range order (S) as a function of Pd concentration (x). Dashed lines are guides for eyes.

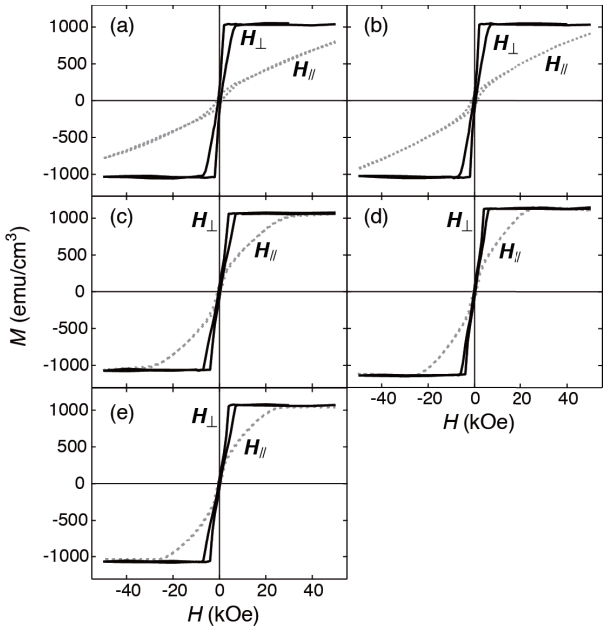

Fig. 3 Magnetization curves for $FePt_{1-x}Pd_x$ films with (a) x = 0, (b) 0.25, (c) 0.5, (d) 0.75, and (e) 1. Solid (dashed) curves are results with field (H) applied perpendicular (parallel) to the film plane.

the cases of ternary alloys, the above factors for the Pt-Pd site were calculated assuming the averaged values with the atomic fractions of Pt and Pd.

The lattice constant of c-axis is gradually reduced as x is increased while a-axis is slightly increased. Consequently, c/a shows a slight decrease with x. The literature values[15] are c = 0.3702 nm and a = 0.3842 nm for FePt, and c = 0.3715 nm and a = 0.3850 nm for FePd, which lead to c/a = 0.964 for FePt and 0.965 for FePd. These reported values do not explain the Pd concentration dependence of lattice constants for the present $FePt_{1-x}Pd_x$ films. The epitaxial strain may be related with the changes in the lattice constants, which depends on the composition and the kind of substrate, although the detailed mechanism has not been understood yet. It is noted that the continuous change in the lattice constants suggests the formation of Fe-Pt-Pd ternary alloy without any phase separation. From Fig. 2 (d), it is confirmed that highly ordered states (S ~ 0.8) are achieved at all the compositions.

Figure 3 shows the magnetization curves for (a) x = 0, (b) 0.25, (c) 0.5, (d) 0.75, and (e) 1, where the solid (dashed) curves are the results with field (H) applied perpendicular (parallel) to the film plane. One sees that the easy magnetization axis is in the normal direction to the film plane for all the films. Namely, all the $FePt_{1-x}Pd_x$ layers are perpendicularly magnetized. However, the saturation field in the in-plane magnetization curve is decreased as x is increased. For example, for x = 0 (FePt), H = 50 kOe is insufficient to saturate the magnetization along the in-plane direction

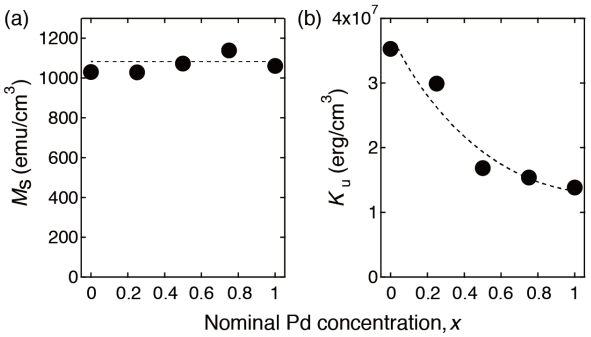

Fig. 4 (a) Saturation magnetization (M_s) and (b) uniaxial magnetic anisotropy energy (K_u) as a function of x. Dashed lines are guides for eyes.

while the magnetization of x = 1 (FePd) saturates even at the in-plane H = 25 kOe. This indicates that the perpendicular magnetic anisotropy is reduced with x.

Figure 4 displays (a) saturation magnetization (M_s) and (b) K_u as a function of x. The value of K_u was calculated from the effective magnetic anisotropy (K_{eff}) with the correction of shape anisotropy energy ($-2\pi M_s^2$), *i.e.* $K_u = K_{eff} + 2\pi M_s^2$. K_{eff} was determined from the area enclosed between the perpendicular and in-plane magnetization curves. In Fig. 4(a), M_s does not show the remarkable composition dependence. A previous paper[1] reported M_s = 1140 emu/cm^3 and 1100 emu/cm^3 for FePt and FePd, respectively, indicating that no remarkable difference in M_s between FePt and FePd. This explains why M_s keeps almost constant regardless of x. On the other hand, K_u shows the significant composition dependence. The largest K_u among the present samples is obtained at x = 0, which is $K_u = 3.5 \times 10^7$ erg/cm^3, and K_u is drastically reduced as x is varied from 0 to 1. The larger K_u for x = 0 than that for x = 1 is consistent with the fact that the bulk FePt shows the larger K_u than the bulk FePd[1]. Our finding is that K_u is monotonically decreased with x for the Fe-Pt-Pd ternary alloys and does not show a local minimum or maximum value.

Next, let us show the results of AHE measurement for the Hall devices with the $FePt_{1-x}Pd_x$ layers. Figure 5 (a) is the transverse resistance (R_{xy}) as a function of H for x = 0, 0.5, and 1, where H was applied along the perpendicular (z) direction to the device plane. The Hall resistivity (ρ_H) is composed of two terms[13]:

$$\rho_H = R_0 H + R_S M(T,H), \quad (2)$$

where $M(T,H)$ is the magnetization averaged over the sample. R_0 and R_S represent the ordinary and anomalous Hall coefficients, respectively. All the devices exhibit clear hysteretic transitions of R_{xy}. The shapes of R_{xy} - H coincide with those of the perpendicular magnetization curves. This means the R_{xy} change originates from the AHE. Figures 5 (b), (c) and (d) summarize the longitudinal conductivity (σ_{xx}), the transverse conductivity (σ_{xy}), and θ_{AHE} as a function of x. θ_{AHE} is defined as $\theta_{AHE} = \sigma_{xy} / \sigma_{xx}$. σ_{xx} (σ_{xy}) increases

(decreases) as x is increased. As a result, x = 0 exhibits the largest θ_{AHE} = 0.04, and θ_{AHE} shows the monotonic reduction down to 0.01 at x = 1. This tendency might be explained by the fact that FePt possesses the spin orbit interaction larger than FePd[16].

Figure 6 displays the AMR effect for the $FePt_{1-x}Pd_x$ layers. The longitudinal resistance (R_{xx}) versus H for x = 0 is shown in Fig. 6(a), where the linear background due to the force effect was subtracted. The solid curve represents the result with H applied along the in-plane current (I), *i.e.* I // H, while the dashed curve represents that with the perpendicular H, *i.e.* $I \perp H$. Thus, the shapes of AMR curves for I // H and $I \perp H$ correspond to the in-plane and perpendicular magnetization curves, respectively. In this study, R_{xx} for I // H ($I \perp H$) are defined as $R_{xx,l}$ ($R_{xx,t}$). As shown in Fig. 6(a), $R_{xx,l}$ is larger than $R_{xx,t}$ for x = 0, which means that the sign of AMR for the FePt is positive. The AMR ratio as a function of x is shown in Fig. 6(b). The definition of AMR ratio in this study is AMR ratio (%) = $(R_{xx,l} - R_{xx,t}) \times 100 / R_{xx,t}$. As x is increased, the AMR ratio is decreased, however a sign reversal of AMR does not occur. The FePt and FePd exhibit 0.8 % and 0.4 % AMR ratios, respectively.

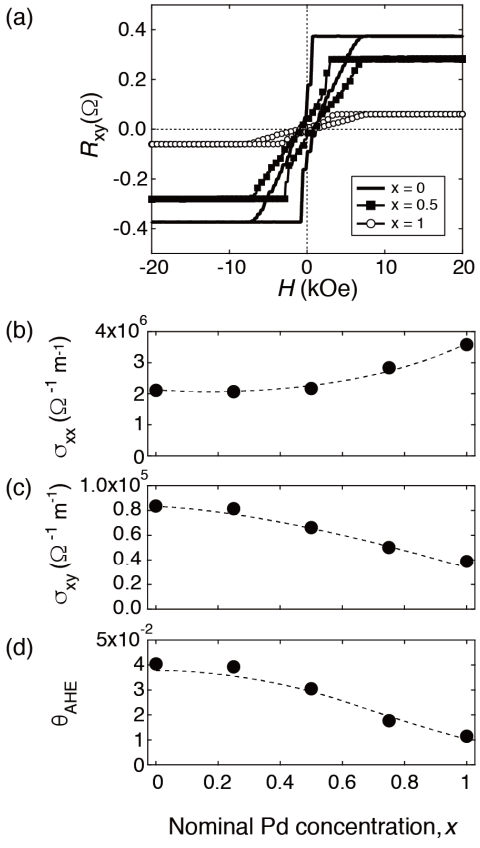

Fig. 5 (a) Transverse resistance (R_{xy}) as a function of H for x = 0, 0.5, and 1, where H was applied along the perpendicular direction to the device plane. (b) Longitudinal conductivity (σ_{xx}), (c) transverse conductivity (σ_{xy}), and (d) θ_{AHE} as a function of x. Dashed lines are guides for eyes.

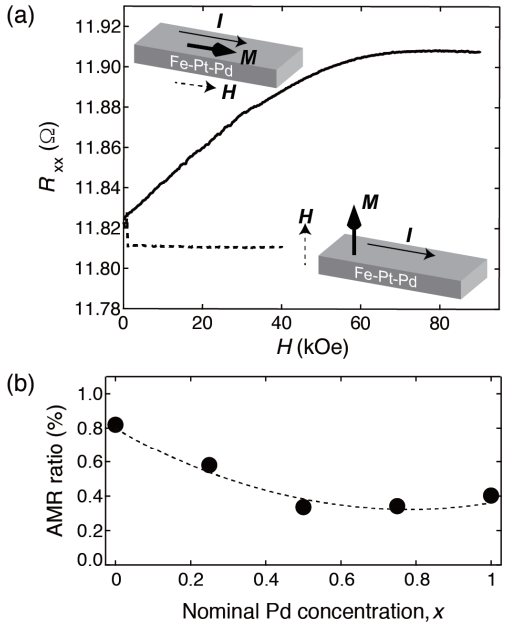

Fig. 6 (a) Longitudinal resistance (R_{xx}) versus H for x = 0. Solid curve represents the result with H applied along the in-plane current (I), *i.e.* I // H, while dashed curve represents that with the perpendicular H, *i.e.* $I \perp H$. (b) AMR ratio as a function of x. Dashed line is guide for eyes.

Here we discuss the composition dependence of θ_{AHE} and AMR ratio for the present $FePt_{1-x}Pd_x$ layers. Seemann and co-workers reported the different scattering mechanisms in AHE between FePt and FePd[10]. According to their experimental study[10], the AHE in FePt is dominated by the intrinsic deflection whereas the side-jump is a dominant mechanism for the FePd. He *et al.* investigated the correlation between the AHE and the spin-orbit coupling parameter[11]. They mentioned that there existed a clear positive correlation between the intrinsic term and the spin-orbit coupling parameter. Since the present composition dependence of θ_{AHE} is similar to the composition dependence of intrinsic term reported in the previous paper[11], the scenario that the spin-orbit coupling dominates the magnitude of AHE is applicable for the present result.

In contrast to AHE, the magnitude of AMR is affected by complicated several factors: spin-orbit coupling constant (λ), exchange field (H_{ex}), and s-d scattering process. According the Campbell-Fert-Jaoul (CFJ) model[17], the AMR of a strong ferromagnet is related with proportional to $(\lambda / H_{ex})^2$, suggesting that large spin-orbit interaction gives rise to the increase of AMR. This may be a simple scenario explaining the present composition dependence of AMR ratio. However, Kokado *et al.* derived the more rigorous model for AMR taking into account the s-d scattering process[14]. In order to completely and quantitatively explain the present result, we need the further consideration.

4. Conclusion

We investigated the composition dependence of AHE and AMR for the $FePt_{1-x}Pd_x$ (001) epitaxial films with highly ordered structures and perpendicular magnetization. Among the present samples, the FePt film exhibited the highest K_u, the largest θ_{AHE}, and the largest AMR ratio. These values were gradually decreased as x was increased. We discussed possible scenarios to explain those composition dependences, suggesting that the spin-orbit interaction plays an important role to determine the magnitude of these values.

Acknowledgements The authors thank Mr. Y. Murakami and Mr. I. Narita for their technical assistance. This work was partially supported by the Grant-in-Aid for Scientific Research S (23226001) and Scientific Research B (16H04487) as well as the Research Grant from the TEPCO Memorial Foundation. The device fabrication and structural characterization were partly performed at Cooperative Research and Development Center for Advanced Materials, IMR, Tohoku University.

References

1) D. Weller, A. Moser, L. Folks, M. E. Best, W. Lee, M. F. Toney, M. Schwickert, J. U. Thiele, and M. F. Doerner. *IEEE Trans. Magn.* **36**, 10 (2000)
2) A. Cebollada, D. Weller, J. Sticht, G. R. Harp, R. F. C. Farrow, R. F. Marks, R. Savoy, and J. C. Scott, *Phys. Rev. B* **50**, 3419 (1994)
3) T. Shima, K. Takanashi, Y. K. Takahashi, and K. Hono, *Appl. Phys. Lett.* **81**, 1050 (2002).
4) S. Okamoto, N. Kikuchi, O. Kitakami, T. Miyazaki, Y. Shimada, and K. Fukamichi, *Phys. Rev. B* **66**, 024413 (2002)
5) M. Ohtake, S. Ouchi, F. Kirino, and M. Futamoto, *J. Appl. Phys.* **111**, 07A708 (2012)
6) T. Seki, S. Mitani, K. Yakushiji, and K. Takanashi, *Appl. Phys. Lett.* **88**, 172504 (2006)
7) S. Mizukami, S. Iihama, N. Inami, T. Hiratsuka, G. Kim, H. Naganuma, M. Oogane, and Y. Ando, *Appl. Phys. Lett.* **98**, 052501 (2011)
8) S. Iihama, A. Sakuma, H. Naganuma, M. Oogane, T. Miyazaki, S. Mizukami, and Y. Ando, *Appl. Phys. Lett.* **105**, 142403 (2014)
9) S. D. Willoughby, J. M. MacLaren, T. Ohkubo, S. Jeong, M. McHenry, D. E. Laughlin, S.-J. Choi, and S.-J. Kwon, *J. Appl. Phys.* **91**, 8822 (2002)
10) K. M. Seemann, Y. Mokrousov, A. Aziz, J. Miguel, F. Kronast, W. Kuch, M. G. Blamire, A. T. Hindmarch, B. J. Hickey, I. Souza, and C. H. Marrows, *Phys. Rev. Lett.* **104**, 076402 (2010)
11) P. He L. Ma, Z. Shi, G.Y. Guo, J.-G. Zheng, Y. Xin, and S. M. Zhou, *Phys. Rev. Lett.* **109**, 066402 (2012)
12) S. Kikushima, T. Seki, K. Uchida, E. Saitoh, and K. Takanashi, *AIP Adv.* **7**, 085210 (2017)
13) N. Nagaosa, J. Sinova, S. Onoda, A. H. MacDonald, and N. P. Ong, *Rev. Mod. Phys.* **82**, 1539 (2010)
14) S. Kokado, M. Tsunoda, K. Harigaya, and A. Sakuma, *J. Phys. Soc. Jpn.* **81**, 024705 (2012)
15) M. Futamoto, M. Nakamura, M. Ohtake, N. Inaba, and T. Shimotsu, *AIP Adv.* **6**, 085302 (2016)
16) Y. Kota, and A. Sakuma, *J. Phys. Soc. Jpn.* **81**, 084705 (2012)
17) I. A. Campbell, A. Fert, and O. Jaoul, *J. Phys. C* **3**, S95 (1970)

Received Oct. 19, 2018; Accepted Dec. 25, 2018

J. Magn. Soc. Jpn., **43**, 34-41 (2019)

<Paper>

Dynamics of magnetization and easy axis of individual ferromagnetic nanoparticle subject to anisotropy and thermal fluctuations

Satoshi Ota and Yasushi Takemura*

Department of Electrical and Electronic Engineering, Shizuoka University, *3-5-1 Johoku, Naka-ku, Hamamatsu 432-8561, Japan*

*Department of Electrical and Computer Engineering, Yokohama National University, *79-5 Tokiwadai, Hodogaya-ku, Yokohama 240-8501, Japan*

In order to design magnetic nanoparticles that are optimized for biomedical applications such as hyperthermia treatment and magnetic particle imaging, their magnetization dynamics should be analyzed. Through conventional analytical methods related to magnetization dynamics such as susceptibility and the magnetization curve, the net properties of magnetization have been previously evaluated. However, an examination of net properties does not yield information related to the stochastic dynamics due to thermal fluctuations and systematic dynamics influenced by the anisotropy with respect to single particles. In this study, the time evolution of the magnetization and easy axis of an individual magnetic nanoparticle was numerically simulated using the Landau-Lifshiz-Gilbert equation in terms of magnetic nanoparticles with fixed and rotatable easy axes, solids and liquids, respectively. The superparamagnetic and ferromagnetic regimes of the Langevin dynamics were clearly discerned through evaluation of the effects of anisotropy and thermal fluctuation, and an index for determining the transition point between these regimes provided. In particular, effects related to the core volume and the anisotropy constant associated with the anisotropy energy were assessed using the Stoner-Wohlfarth model.

Key words: magnetic nanoparticles, anisotropy energy, thermal energy, easy axis

1. Introduction

Magnetization dynamics in magnetic nanoparticles (MNPs) were important to develop biomedical application. MNPs are used as a heat source for hyperthermia [1] and as a tracer for magnetic particle imaging (MPI) [2]. In general, with respect to hyperthermia, heat dissipation is derived from the energy losses such as hysteresis and magnetic relaxation losses. The hysteresis loss is due to the presence of the ferromagnetic regime of the MNPs, which in turn is derived from the anisotropy of the magnetization along the easy axis. The magnetic relaxation loss is related to the hysteresis associated with the time delay of the magnetization response from the applied field. This hysteresis loss that is due to anisotropic effects and magnetic relaxation also affects the harmonic response of the magnetization that is crucial for MPI.

In order to evaluate magnetization dynamics, the AC susceptibility [3–6] and AC magnetization curve [7–9] have been previously determined. In addition, the specific loss power and the intrinsic loss power [10–13] for hyperthermia, the magnetic particle spectrometry signal [14], and the harmonics of the magnetization [15–17] for MPI have been assessed. Theoretical and numerical simulations focusing on AC susceptibility and AC magnetization curves have also revealed the dynamics of magnetization [18–21] and the easy axis [22,23] with respect to magnetic relaxation.

Magnetic relaxation is divided into Néel and Brownian relaxations, referring to relaxations of the magnetization and the easy axis, respectively. In terms of conventional theory, magnetic relaxation occurs in accordance with the theory of the effective relaxation time τ_{eff}, given by $1/\tau_{eff} = 1/\tau_N + 1/\tau_B$, where τ_N and τ_B are the Néel and Brownian relaxation times, respectively [18]. This conventional theory indicated the dominance of one type of relaxation, with one relaxation time shorter than the other. However, the superimposition of the Néel and Brownian relaxations has been observed using numerical simulations [22] and magnetization measurements [24]. In our previous study, increases in magnetization derived from the Brownian relaxation in addition to the Néel relaxation were measured when applying a pulse field [25]. Moreover, the dynamics of the easy axis of MNPs in a liquid was estimated using the subtracted magnetization curve indicating the difference between the measured magnetization curve in a solid and that in a liquid [26].

Through an analysis of susceptibility and the magnetization curve, their dynamics in terms of individual particles remain unclear, although the net properties of the magnetization and easy axis are evaluated. García-Palacios and Lázaro observed the trajectories of individual magnetization using the Langevin-dynamics approach, which indicated the presence of magnetization reversal properties associated with anisotropy and thermal fluctuation [27]. Lopez-Diaz *et al.* showed that the transition of magnetism depended on particle size, in terms of the switching responses of typical individual magnetizations [28]. In this study, using numerical simulation methods that employ the Landau-Lifshiz-Gilbert (LLG) equation, the dynamics of magnetization and the easy axis were evaluated by focusing on single particle trajectories in conditions with fixed and rotatable easy axes, i.e., a solid and a fluid, respectively. The effects of the uniaxial anisotropy along the easy axis and thermal fluctuation at the transition from the superparamagnetic regime represented by stochastic Langevin dynamics to the ferromagnetic

regime given by the Stoner-Wohlfarth model [29] were assessed. This single particle model reveals the effects of anisotropy and thermal fluctuations in the superparamagnetic and ferromagnetic regimes.

2. Numerical simulation

2.1 Simulated materials

Monodispersed single-domain MNPs were considered in the numerical simulation. The interparticle dipole interaction was ignored, and the hydrodynamic diameters d_h of the MNPs was equal to their core diameters d_c. The effective uniaxial anisotropy constants K_u were 8, 9.8, 12, 14.7, and 18 kJ/m^3 with d_c of 11 nm. In addition, with respect to the case for which K_u was equal to 12 kJ/m^3, d_c of 9.61, 10.3, 11.8, and 12.6 nm were used. These parameters were considered for the evaluation of the magnetization dynamics and depended on the ratio of the anisotropy energy to the thermal energy, $\xi = K_u V_M / k_B T$, where V_M is the volume of a core particle, k_B is the Boltzmann constant (1.38×10^{-23} J/K), and T is the temperature, set to 300 K (Table 1). The saturation magnetic moment M_s was 269 kA/m, which was taken from the information related to the material measured in Ref. 24).

2.2 Simulation methods

The dynamics of magnetization in the case of a rotatable easy axis such as the MNPs in a fluid are calculated using the modified LLG equation[21),23)]. In a fluid, the dynamics of the easy axis is considered in addition to the magnetization dynamics. The orientation of the easy axis is calculated using the unit vector and the angular velocity of the easy axis, $\mathbf{n}$ and $\boldsymbol{\omega}$, respectively, as follows:

$$\frac{d\mathbf{n}}{dt} = \boldsymbol{\omega} \times \mathbf{n}. \tag{1}$$

The differential equation of the angular velocity of the easy axis is given by [21)]

$$\Theta \frac{d\boldsymbol{\omega}}{dt} = \frac{\mu_0 M_s V_M}{\gamma} \frac{d\mathbf{m}}{dt} + \mu_0 M_s V_M \mathbf{m} \times (\mathbf{H}_{ex} + \mathbf{H}_{th}) - \kappa \boldsymbol{\omega} + \Gamma_{th}, \tag{2}$$

where Θ is the moment of inertia, μ_0 is the permeability of free space, γ is the gyromagnetic ratio, $\mathbf{m}$ is the magnetic moment normalized by the saturation magnetic moment, $\mathbf{H}_{ex}$ is the excitation field, $\mathbf{H}_{th}$ is thermally fluctuating field, κ is the friction coefficient, $\boldsymbol{\Gamma}_{th}$ is random torque due to thermal fluctuation. γ is estimated to be $\gamma = \mu_0 M_s V_M (1+\alpha^2)/(2\alpha\tau_N k_B T)$ where $\tau_N = \pi^{1/2}\tau_0 \exp(\xi)/2\xi^{1/2}$ [30)]. κ is expressed as $\kappa = 6\eta V_H$ where η is the medium viscosity, set to 0.89 mPa·s, and V_H is the particle hydrodynamic volume. $\mathbf{H}_{th}$ and $\boldsymbol{\Gamma}_{th}$ have Gaussian distributions with a zero mean. The variance of $\mathbf{H}_{th}$ and $\boldsymbol{\Gamma}_{th}$ satisfied the following equations:

$$\langle H_{th,i}(t) H_{th,j}(t') \rangle = \frac{2\alpha}{1+\alpha^2} \frac{k_B T}{\gamma \mu_0 M_s V_M} \delta_{ij} \delta(t-t'), \tag{3}$$

$$\langle \Gamma_i(t) \Gamma_j(t') \rangle = 2\kappa k_B T \delta_{ij} \delta(t-t'). \tag{4}$$

In Eqs. (3) and (4), i and j are the Cartesian indices of different particles, and δ_{ij} is the Kronecker delta function, and δ is the Dirac delta function.

Here, with respect to $\boldsymbol{\omega}$, the inertial effects can be ignored, and $\mu_0 M_s V_M / \gamma$ is extremely small. Thus, Eq. (2) is rewritten as the equation of $\boldsymbol{\omega}$, as follows:

Table 1 The anisotropy constant K_u and the core diameter d_c of the numerically simulated MNPs. K_u was equal to 8, 9.8, 12, 14.7, and 18 kJ/m^3 with d_c= 11nm. For K_u=12 kJ/m^3, d_c was 9.61, 10.3, 11, 11.8, and 12.6 nm, where the ratios of the anisotropy energy to the thermal energy $\xi = K_u V_M / k_B T$ were 1.35, 1.65, 2.02, 2.47, and 3.03, respectively.

K_u [kJ/m^3] (d_c= 11 nm)	8	9.8	12	14.7	18
d_c [nm] (K_u= 12 kJ/m^3)	9.61	10.3	11	11.8	12.6
ξ	1.35	1.65	2.02	2.47	3.03

$$\boldsymbol{\omega} = \frac{1}{\kappa} \{ \mu_0 M_s V_M \mathbf{m} \times (\mathbf{H}_{ex} + \mathbf{H}_{th}) + \Gamma_{th} \}. \tag{5}$$

When the magnetization is entirely bound to the easy axis represented by Eq. (1), the dynamics of the magnetization is given by

$$\frac{d\mathbf{m}}{dt} = \boldsymbol{\omega} \times \mathbf{m}. \tag{6}$$

In addition to the term influenced by the rotation of the easy axis in Eq. (6), the magnetization dynamics is represented by the damping process according to the conventional LLG equation [31)], as follows:

$$\begin{aligned} \frac{d\mathbf{m}}{dt} = \boldsymbol{\omega} \times \mathbf{m} - \frac{\gamma}{1+\alpha^2} \mathbf{m} \times \left(\mathbf{H}_{eff} + \mathbf{H}_{th} - \frac{\boldsymbol{\omega}}{\gamma} \right) \\ - \frac{\alpha\gamma}{1+\alpha^2} \mathbf{m} \times \left\{ \mathbf{m} \times \left(\mathbf{H}_{eff} + \mathbf{H}_{th} - \frac{\boldsymbol{\omega}}{\gamma} \right) \right\}, \end{aligned} \tag{7}$$

where α is damping parameter (α= 0.1), $\mathbf{H}_{eff}$ is effective field composed of $\mathbf{H}_{ex}$ and anisotropy field ($\mathbf{H}_{an}$). The anisotropy field is estimated to be $\mathbf{H}_{an} = 2K_u(\mathbf{m} \cdot \mathbf{n})\mathbf{n}/(\mu_0 M_s)$. $\boldsymbol{\omega}/\gamma$ indicates the field derived from the rotation of the easy axis.

In the case of the model with a fixed easy axis, the term including $\boldsymbol{\omega}$ in Eq. (7) was omitted. For the numerical simulations, the differential equations were solved with the Runge–Kutta method. In the numerical simulations used for the analysis of the net magnetization dynamics, there were 29440 particles. The excitation AC field was applied along the x-axis with the amplitude H_{max} of 8 kA/m and the frequency f of 10 kHz except for the frequency dependence analysis.

2.3 Time evolution of magnetization and easy axis orientations

The magnetization and easy axis orientations were observed during the half cycle for a phase of 0–π in an applied AC field, $H_{max}\cos(2\pi ft)$, where t is the time. The chosen time interval was 100 ns. Because the dynamics of the individual magnetization and easy axis are subject to fluctuations caused by thermal disturbances and therefore show variance, it is necessary to confirm the statistical accuracy of these simulations. With respect to the statistical analysis, the magnetization and easy axis orientations were evaluated in one cycle. The number of particles N was 100.

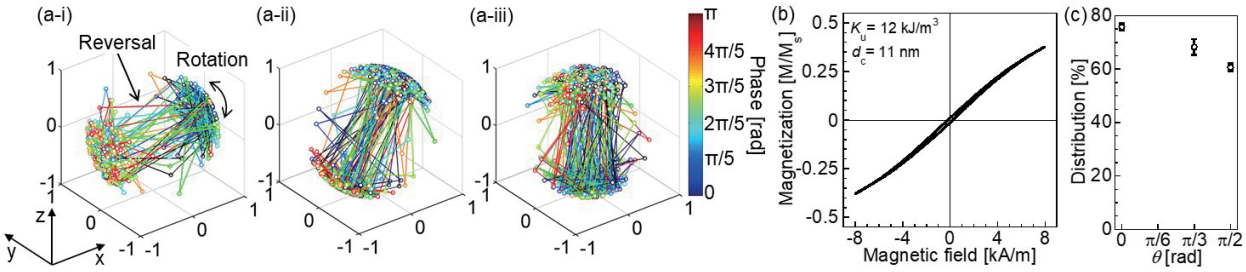

Fig. 1 Time evolutions of individual magnetization orientation in the spherical model for the MNP with K_u= 12 kJ/m^3 and d_c= 11 nm, with the easy axis fixed along (a-i) θ= 0 rad, (a-ii) θ= π/3 rad, and (a-iii) θ= π/2 rad in the x-z plane. The lines over the y-z plane perpendicular to the applied field along the x-axis indicate the reversal of the magnetization, and other lines represent the rotation of the magnetization. (b) Magnetization curve and (c) distribution of the magnetization orientation along the applied field direction on the x-axis for the MNP illustrated in (a-i)–(a-iii). The statistical analysis was conducted in one cycle of the applied field, with a time interval of 100 ns (N= 100).

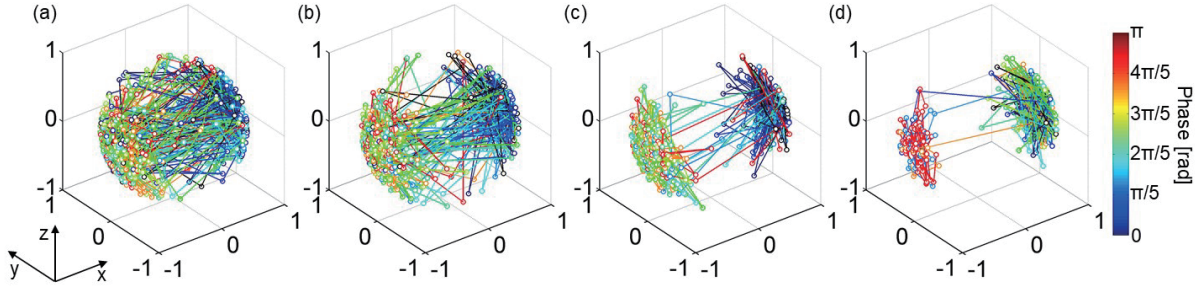

Fig. 2 Time evolutions of individual magnetization orientations in the spherical model for the MNP with (a) K_u= 8, (b) 9.8, (c) 14.7, and (d) 18 kJ/m^3 with d_c= 11 nm, with the easy axis fixed along θ= 0 rad.

3. Results and discussions

3.1 Dynamics of magnetization with a fixed easy axis

3.1.1 Effect of easy axis direction

Figure 1 shows the time evolutions of the individual magnetization orientation in the three-dimensional model with respect to a MNP of K_u= 12 kJ/m^3 and d_c= 11 nm. The easy axis was oriented so that the angle between the easy axis and the applied field was θ= 0, π/3, and π/2 rad in the x-z plane in Figs. 1(a-i)–(a-iii), respectively. On the basis of the Stoner-Wohlfarth model, the magnetization was distributed around the easy axis and along the direction of the applied field because of low potential energy [20),29)].

Figure 1(b) shows the magnetization curve of the MNP with K_u= 12 kJ/m^3 and d_c= 11 nm. A slight coercivity indicates ferromagnetism. The distribution of the magnetization along the same direction as the applied field is evidenced in Fig. 1(c). With decreasing θ, the magnetization distribution was strongly aligned along the direction of the applied field, owing to the reduced anisotropy energy barrier [9),32),33)]. Two nodes connected by a line show the continuous trajectory of the magnetization in Fig. 1(a). The lines over the y-z plane perpendicular to the applied field indicate the magnetization reversal, while other lines represent the rotation of the magnetization. Random oscillations in the magnetization including frequent reversals and rotations were due to thermal fluctuations resulting from the superparamagnetism.

3.1.2 Dependence of the anisotropy constant and core diameter

Figure 2 shows the time evolutions of the individual magnetization depending on K_u, with d_c= 11 nm. The magnetization reversals that are due to thermal fluctuations were suppressed by the large anisotropy energy. Moreover, in contrast to the spreading of the magnetization along the spherical surface in the small-K_u regime, the distribution of the magnetization was concentrated on the direction of the easy axis for large ξ. The magnetization was strongly bound by the anisotropy.

The ratio of the magnetization reversal in the trajectories was confirmed in Fig. 3. According to the time evolution shown in Fig. 2, the magnetization reversal that was due to the thermal noise was suppressed by the large anisotropy energy. When d_c was increased with K_u= 12 kJ/m^3, the magnetization reversal ratio decreased because of the increase in the anisotropy energy, which is similar to the case in which K_u increased with d_c= 11 nm. However, the magnetization reversal ratios for each ξ were statistically larger than for the case of large d_c despite the same ξ values (Table 1). The p-values were $p < 0.01$ in $\xi \leq 2.47$ and $p < 0.1$ in ξ= 3.03.

The potential energy E_p is given by

$$E_p = K_u V_M \sin^2(\theta - \varphi) - \mu_0 M_s V_M |\mathbf{H}_{ex}| \cos(\varphi), \quad (8)$$

where φ is the angle between the magnetization and the applied field [29)]. The first and second terms in Eq. (8) are the anisotropy and Zeeman energies, respectively.

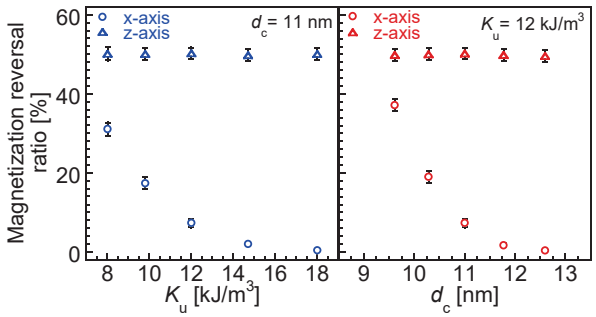

Fig. 3 Ratio of the magnetization reversal represented over the y-z plane along the x-axis and the x-y plane along the z-axis for the all the magnetization trajectories. K_u and d_c for the MNPs were shown in Table 1. The easy axis was fixed on the x-axis. The statistical analysis was conducted within one cycle of the applied field with a time interval of 100 ns (N= 100).

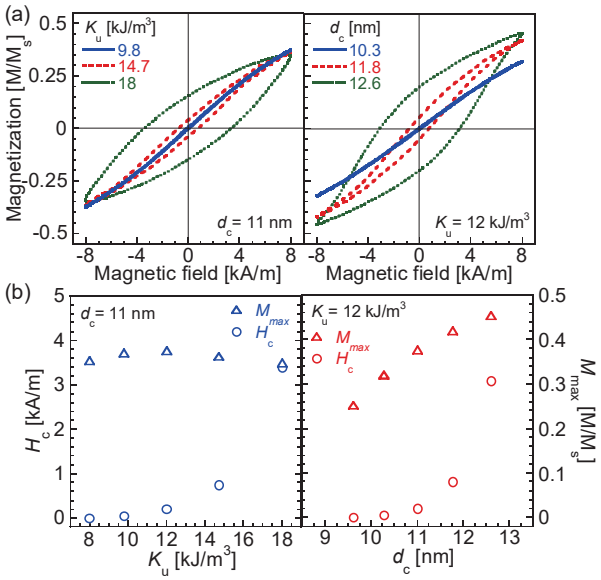

Fig. 4 (a) Magnetization curve and (b) the maximal magnetization M_{max}, and coercivity H_c depending on K_u and d_c, shown in Table 1. The easy axis was fixed on the x-axis.

An increase of d_c enhances the amplitude of both the anisotropy and Zeeman energies, whereas K_u affects only the anisotropy energy. The effect of d_c on the Zeeman energy is similar with that of $|\mathbf{H}_{ex}|$ in the Stoner-Wohlfarth model [34]. Thus, the effectively large $|\mathbf{H}_{ex}|$ in addition to the large anisotropy inhibited magnetization reversal due to thermal noise in the case of a large d_c for the same ξ. The magnetization reversal along the z-axis was also evaluated in Fig. 3. However, the reversal ratio was independent of the anisotropy energy because the easy axis associated with the uniaxial anisotropy and the applied field were perpendicular to the z-axis, and only random thermal fluctuations affected the magnetization oscillation.

Figures 4(a) and (b) show the magnetization curves, and the dependence of the maximal magnetization M_{max} and coercivity H_c on K_u and d_c. H_c was increased by the large anisotropy energy. The hysteresis associated with H_c in ξ= 3.03 was particularly large. In a solid, the hysteresis is due to pinning of the magnetization to the easy axis and the phase delay derived from the Néel relaxation. In ξ= 3.03, because the Néel relaxation time is short compared to the frequency of the applied field, the hysteresis is dominantly due to pinning of the magnetization by the large anisotropy energy barrier. For the same ξ values, H_c was equal with each other for $\xi \leq 2.47$. However, H_c in K_u= 18 kJ/m^3 and d_c= 11 nm was larger than that in the case of K_u= 12 kJ/m^3 and d_c= 12.6 nm in ξ= 3.03, because Zeeman energy enough for the magnetization to reverse is similar with each other. The magnetization overcoming the energy barrier was reduced by the small Zeeman energy in the case of ξ= 3.03. The decrease of M_{max} for $K_u \geq$ 12 kJ/m^3 and d_c= 11 nm was also associated with the large anisotropy energy barrier and the unchanged Zeeman energy. M_{max} increased with increasing d_c where K_u= 12 kJ/m^3 because of the presence of high Zeeman energy.

3.1.3 Transition in the magnetic regime

As shown in Fig. 2, the change in the anisotropy energy induces the transition from the superparamagnetic regime, the stochastic aspect of the Langevin dynamics, to the ferromagnetic regime, their energetically systematic aspect shown by the Stoner-Wohlfarth model [28]. The Langevin equation describing the system of time evolution for the magnetization is generalized as

$$\frac{d\mathbf{m}(t)}{dt} = A(\mathbf{m}(t)) + F(t), \tag{9}$$

where the function $A(\mathbf{m}(t))$ represents the systematic term that represents the potential energy and the function $F(t)$ is the term that describes fluctuations that are due to thermal disturbance [27),35]. Where the fluctuating term dominates, the magnetization dynamics clearly place the system in the superparamagnetic regime.

Figure 5 shows the dependence of the energy ratio E_p/k_BT on φ by Eq. (8). The large anisotropy in the superparamagnetic regime prevents the most energetically stable magnetization from reversion to the metastable condition by overcoming the anisotropy energy barrier through thermal fluctuations. Here, the

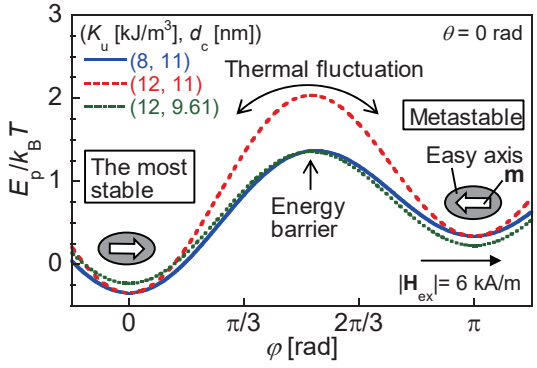

Fig. 5 Potential energy normalized by the thermal energy, E_p/k_BT with respect to φ with the easy axis fixed along θ= 0 rad. (K_u, d_c) were (8 kJ/m^3, 11 nm), (12 kJ/m^3, 11 nm), and (12 kJ/m^3, 9.61 nm), where ξ= 1.35, 2.02, and 1.35, respectively. The intensity of the applied field $|\mathbf{H}_{ex}|$ was 6 kA/m.

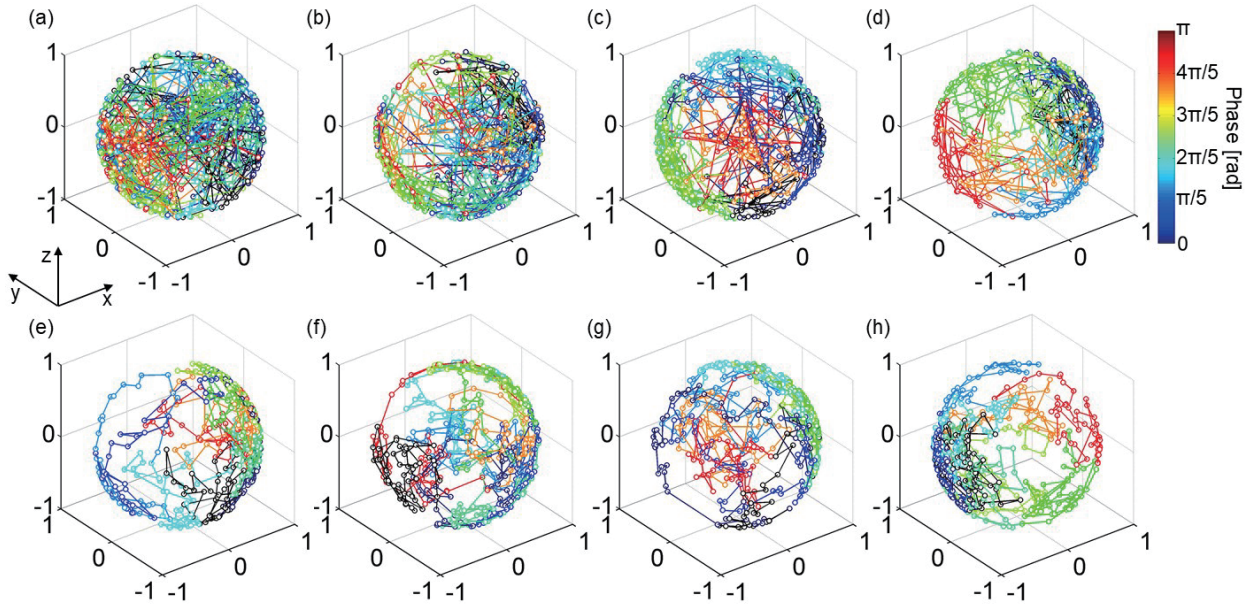

Fig. 6 Time evolutions of the individual orientations of the (a–d) magnetization and (e–h) rotatable easy axis in the spherical model with respect to the MNP with (a, e) K_u= 9.8, (b, f) 12, (c, g) 14.7, and (d, h) 18 kJ/m^3 with d_c= 11 nm.

energy barrier is defined as the maximal value of E_p/k_BT and is enlarged along with the increments of K_u. At the same ξ value, with large d_c and an unchanged energy barrier height, E_p/k_BT is increased and decreased in the metastable and the most stable conditions, respectively (Fig. 5). When d_c was increased, the magnetic moment was monotonically increased in $\xi \leq 3.03$ because energetic stability was enhanced and reduced in the most stable and metastable conditions, respectively (Fig. 4(b)). The inverse reversal into the metastable condition that was due to the thermal disturbance in the superparamagnetic regime was suppressed by the high energy barrier, which led to an increased probability of bound magnetization in the most stable condition. By contrast, in the ferromagnetic regime at large K_u, the high energy barrier inhibits magnetization reversal from the metastable to the most stable conditions because both the minimal and secondary minimal potential energies were unchanged, which results in a reduced M_{max}. Thus, the plotted dependence of M_{max} on K_u showed a peak at K_u= 12 kJ/m^3 (Fig. 4(b)). The value of ξ at the M_{max} peak is the index of the energetic threshold of the transition from the superparamagnetic regime to the ferromagnetic regime in the Langevin dynamics described by Eq. (9).

3.2 Magnetization dynamics with a rotatable easy axis

3.2.1 Trajectories of individual magnetization and easy axis

Figure 6 shows the time evolutions of the individual magnetization and the rotatable easy axis depending on K_u for d_c= 11 nm. For $K_u \leq 12$ kJ/m^3 ($\xi \leq 2.02$), as an effect of thermal fluctuations, the easy axis was randomly rotated along the spherical surface, while fluctuating magnetization reversal occurred. For $K_u \geq 14.7$ kJ/m^3 ($\xi \geq 2.47$), both the magnetization and the easy axis were rotated along the spherical surface.

The anisotropy energy bound the magnetization to the rotatable easy axis, as in the case of the fixed easy axis. The angle between the magnetization and the easy axis ψ was evaluated for the individual particles. ψ was calculated from the vector product between the unit vector of the magnetization and the easy axis, $|\mathbf{m} \times \mathbf{n}|$. Origin symmetry is applicable for the easy axis (Eq. (8)). The averaged value of ψ shown in Fig. 7 indicates that ψ was reduced with a large anisotropy energy with the increase of both K_u and d_c. Therefore, considering the magnetization dynamics in a fluid, the reduction in the anisotropy energy barrier implies that the particles exhibit superparamagnetic behavior in the ferromagnetic regime, which is empirically confirmed by the reduced coercivity in a fluid compared with that in a solid on the DC magnetization curve [24]. This may be distinguished from the superparamagnetic regime as the effect of thermal fluctuations is reduced in the case of MNPs due to the large anisotropy energy.

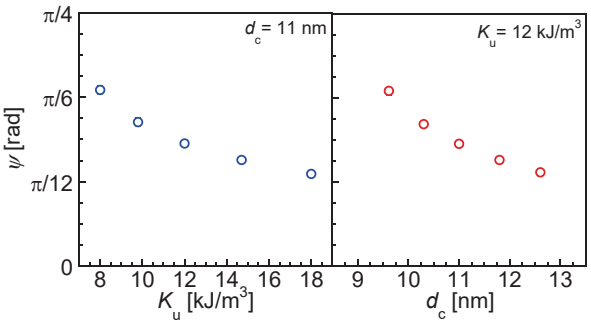

Fig. 7 Angle between the magnetization and the easy axis ψ depending on the anisotropy energy for the K_u and d_c values shown in Table 1. The easy axis was rotatable. ψ was calculated using the expression $|\mathbf{m} \times \mathbf{n}|$. The statistical analysis was conducted in one cycle of the applied field with a time interval of 100 ns (N= 100).

3.2.2 Properties of net magnetization

Figures 8(a) and (b) show magnetization curves, and their corresponding M_{max} and H_c, which increased with increasing ξ. High d_c values corresponded to a high M_{max}, for the same ξ values. This was indicated by the large Zeeman energy that corresponded to large d_c, as in the case of the fixed easy axis (Eq. (8)). In the case of the rotatable easy axis, because the MNPs exhibit superparamagnetic behavior, the H_c derived from the hysteresis that was due to the anisotropy energy barrier is marginal. At high frequencies, the increase in H_c is associated with the phase delay derived from the magnetic relaxations. The magnetic torques $\Gamma_M = \mu_0 M_s V_M |\mathbf{m}\times\mathbf{H}_{ex}|$ that were included in the first term of Eq. (5) depended on both K_u and d_c. Figure 9 shows the ratio of the maximum value of the magnetic torque $\Gamma_{M,max}$ to the thermal energy, $\Gamma_{M,max}/k_BT$. $\Gamma_{M,max}$ increased with increasing K_u ($\xi \leq 2.02$) and saturated in $2.02 \leq \xi \leq 3.03$. The dependence of magnetic torque on K_u has been confirmed by Carrey and Hallali [36]. Γ_M is proportional to V_M and increases for large d_c. The large anisotropy energy enhances Γ_M and affects the Brownian relaxation time. Yoshida and Enpuku took account of the AC field amplitude H_{ac} associated with magnetic torque, describing an effective Brownian relaxation time, $\tau_{B,eff} = \tau_B/[1+0.07(\mu_0 M_s H_{ac}/k_B T)]^{1/2}$, where $\tau_B = 3\eta V_H/k_B T$ [37]. Mamiya and Jeyadevan also indicated the effect of magnetic torque on the Brownian relaxation time [22]. According to these conventional studies, the Brownian relaxation time is reduced due to the large magnetic torque, which induces a small H_c. Usadel also showed that the phase delay of the magnetization in a viscous liquid was reduced in the case of a large field amplitude [21]. In Fig. 8, H_c was negligible for small K_u ($\leq$ 9.8 kJ/m^3) where $d_h = d_c$ = 11 nm, which indicates that the phase delay of the magnetization derived from the Brownian relaxation was negligible. Thus, H_c increased for large K_u where d_c = 11 nm, which was due to the phase delay of the magnetization derived from only the Néel relaxation. In addition, H_c increased with increasing d_c at K_u = 12 kJ/m^3, which was due to the phase delay related to the Néel relaxation [18] because H_c values were the same for the same ξ ($\leq$ 2.47). On the other hand, in the case for which K_u = 12 kJ/m^3 and $d_h = d_c$ = 12.6 nm, H_c was larger than that when K_u = 18 kJ/m^3 and d_c = 11 nm because of the phase delay associated with Brownian relaxation.

3.3 Frequency dependence of magnetization and easy axis dynamics

Figure 10(a) shows the time evolutions of the individual magnetization at f = 1 kHz and 100 kHz. The time evolution at f = 10 kHz is shown in Fig. 1(a-i). The magnetization reversals that are due to thermal fluctuations was suppressed with the increasing field frequency, which is indicated in Fig. 10(b). The frequency dependence of the magnetization curves in Fig. 10(c) shows the increasing H_c with increasing field frequency due to the phase delay of the magnetization associated with the Néel relaxation. In the high frequency, the magnetization dynamics correspond to the ferromagnetic regime. The remanent magnetizations without overcoming the energy barrier along the easy axis in the high frequency are

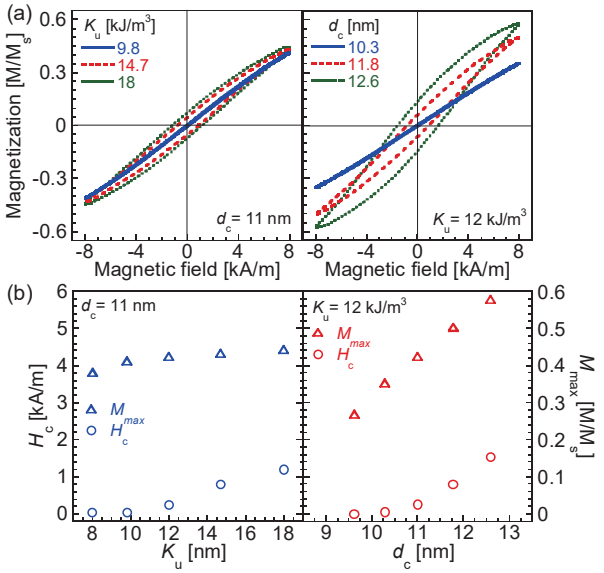

Fig. 8 (a) Magnetization curve and (b) the maximal magnetization M_{max}, and coercivity H_c depending on the anisotropy energy for each K_u and d_c value shown in Table 1. The easy axis was rotatable.

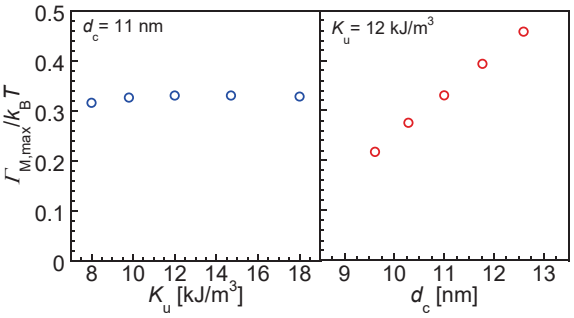

Fig. 9 Maximal magnetic torque normalized by the thermal energy, $\Gamma_{M,max}/k_BT$, depending on the anisotropy energy, for each K_u and d_c value shown in Table 1.

represented as the increases of the phase delay and H_c in the net magnetization properties.

In the case of the rotatable easy axis, the time evolutions of the individual magnetization and easy axis at f = 1 kHz and 100 kHz are shown in Fig. 11(a). The time evolution at f = 10 kHz is shown in Fig. 6(b, f). Figure 11(b) shows the frequency dependence of the magnetization curves and the mean orientation of the easy axis, $\langle\cos\theta\rangle$. At f = 1 kHz, H_c of the magnetization curve and the hysteresis of the easy axis was negligible. The slight H_c confirmed at 10 kHz was derived from the Néel relaxation because this H_c value was similar to the H_c in the case of the fixed easy axis. At 100 kHz, H_c in the case of the rotatable easy axis was larger than for the case of the fixed easy axis, which is described as the phase delay derived from the Brownian relaxation. In particular, the minimum value of $\langle\cos\theta\rangle$ at 100 kHz was higher than 0.5, which indicates that the easy axis was steadily oriented along the applied field direction [23]. The time evolution of the easy axis also illustrated the rotation with the orientation toward the specific direction at 100 kHz, whereas the easy axis was

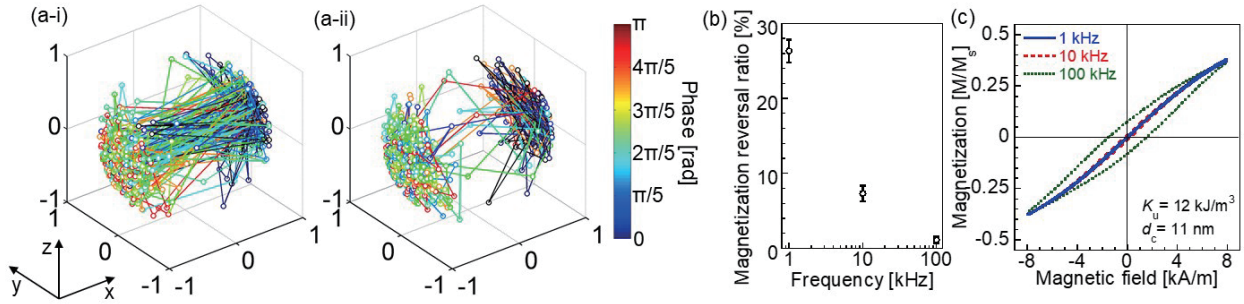

Fig. 10 Time evolutions of the individual magnetization orientation in the spherical model for the MNP with K_u= 12 kJ/m^3 and d_c= 11 nm with the easy axis fixed along θ= 0 at the field frequency of (a-i) 1 kHz and (a-ii) 100 kHz. (b) Ratio of the magnetization reversal represented over the y-z plane along the x-axis and (c) magnetization curve in the frequency of 1–100 kHz. The statistical analysis was conducted in one cycle of the applied field, with a time interval of 100 ns (N= 100).

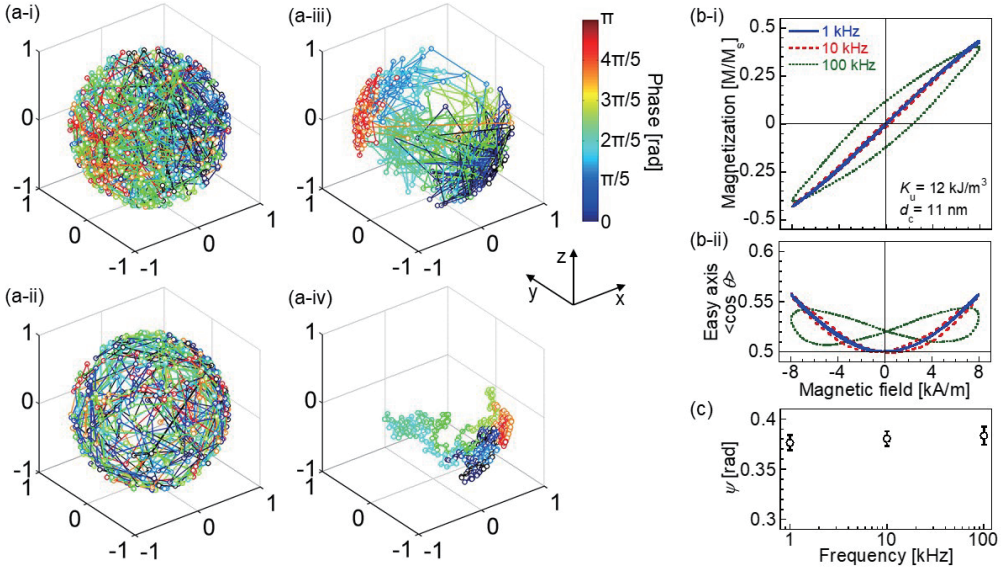

Fig. 11 Time evolutions of the individual (a-i, iii) magnetization and (a-ii, iv) rotatable easy axis orientation in the spherical model for the MNP of K_u= 12 kJ/m^3 and d_c= 11 nm at the field frequency of (a-i, ii) 1 kHz and (a-iii, iv) 100 kHz. (b-i) Magnetization curve, (b-ii) easy axis orientation <cos θ>, and (c) ψ in the frequency of 1–100 kHz. The statistical analysis was conducted in one cycle of the applied field, with a time interval of 100 ns (N= 100).

randomly orientated over the spherical surface at 1 kHz and 10 kHz. At 100 kHz, the magnetization was oriented along the easy axis toward the specific direction and was rotated on the spherical surface, which is similar to the case of the large ξ at 10 kHz in Fig. 6. The transition from the superparamagnetic behavior in the low frequency to the ferromagnetic behavior in the high frequency was observed in the case of the rotatable easy axis. Though ψ increased with increasing frequency, the increased value was slight in Fig. 11(c), which indicates that the magnetization dynamics show the ferromagnetic regime regardless of the field frequency at K_u= 12 kJ/m^3 and d_c= 11 nm. It is observed that the frequency no longer affected the magnetic regime whereas the magnetic behavior was influenced by the frequency.

4. Conclusion

The dynamics of individual particle magnetization and the easy axis were evaluated for the three-dimensional trajectories of a single MNP using numerical simulation. In this paper, the effects of the core size and anisotropy of MNPs on the magnetization and easy axis dynamics were revealed in the same anisotropy energy. For the MNP in a solid (fixed easy axis) model, the ratio of the anisotropy energy to the thermal energy acts as the index of the threshold for the transition from the superparamagnetic to the ferromagnetic regime, considering the effects of stochastic thermal fluctuations and the potential energy of the MNP based on the Stoner-Wohlfarth model. In a fluid (rotatable easy axis), depending on the anisotropy energy, the dynamics of the magnetization and the easy axis changed from that of steep reversal to rotation on the spherical surface, which was associated with the transition from the superparamagnetic to the ferromagnetic regime. The net magnetization shown in the magnetization curves indicates superparamagnetic behavior in the case of the rotatable easy axis, while the ferromagnetic regime was clearly observed when examining the trajectories of the

single MNP. The specific magnetic behavior in a fluid was clearly distinguished from the magnetic regime by the observation of the individual MNP. The magnetic regime in a fluid was illustrated as the difference between the reversal and rotation in the magnetization dynamics. Moreover, it is also statistically revealed that the traceability of the easy axis to the magnetization in a fluid is enhanced in large anisotropy energy. The transition of the magnetic behavior depending on the applied field frequency was also confirmed. However, it is of note that the magnetic regime based on the potential energy was no longer influenced by the frequency. This evaluation of the dominance of superparamagnetic and ferromagnetic regimes in the stochastic Langevin dynamics of the system that depends on the anisotropy energy and thermal fluctuations contributes to the optimal material design of MNPs for use in biomedical applications such as hyperthermia treatment and MPI.

Acknowledgements This work was partially supported by the JSPS KAKENHI Grant Numbers 15H05764, 17H03275, 17K14693.

References

1) A. Jordan, R. Scholz, P. Wust, H. Fähling, R. Felix: *J. Magn. Magn. Mater.*, **201**, 413–419 (1999).
2) B. Gleich and J. Weizenecker: *Nature*, **435**, 1214–1217 (2005).
3) P. C. Fannin, B. K. P. Scaife, and S. W. Charles: *J. Phys. D: Appl. Phys.*, **21**, 533–534 (1988).
4) R. Hergt, R. Hiergeist, I. Hilger, W. A. Kaiser, Y. Lapatnikov, S. Margel, U. Richter: *J. Magn. Magn. Mater.*, **270**, 345–357 (2004).
5) M. Suto, Y. Hirota, H. Mamiya, A. Fujita, R. Kasuya, K. Tohji, and B. Jeyadevan: *J. Magn. Magn. Mater.*, **321**, 1493–1496 (2009).
6) S. B. Trisnanto and Y. Kitamoto: *Phys. Rev. E*, **90**, 032306 (2014).
7) H. Kobayashi, A. Hirukawa, A. Tomitaka, T. Yamada, M. Jeun, S. Bae, and Y. Takemura: *J. Appl. Phys.*, **107**, 09B322 (2010).
8) D. Cabrera, J. Camarero, D. Ortega, and F. J. Teran: *J. Nanopart. Res.*, **17**, 121 (2015).
9) S. A. Shah, D. B. Reeves, R. M. Ferguson, J. B. Weaver, and K. M. Krishnan: *Phys. Rev. B*, **92**, 094438 (2015).
10) S. Dutz, J. H. Clement, D. Eberbeck, T. Gelbrich, R. Hergt, R. Müller, J. Wotschadlo, M. Zeisberger: *J. Magn. Magn. Mater.*, **321**, 1501–1504 (2009).
11) M. Kallumadil, M. Tada, T. Nakagawa, M. Abe, P. Southern, Q. A. Pankhurst: *J. Magn. Magn. Mater.*, **321**, 1509–1513 (2009).
12) E. Kita, T. Oda, T. Kayano, S. Sato, M. Minagawa, H. Yanagihara, M. Kishimoto, C. Mitsumata, S. Hashimoto, K. Yamada, and N. Ohkohchi: *J. Phys. D: Appl. Phys.*, **43**, 474011 (2010).
13) S. Ota, T. Yamada, and Y. Takemura: *J. Nanomater.*, **2015**, 836761 (2015).
14) S. A. Shah, R. M. Ferguson, and K. M. Krishnan: *J. Appl. Phys.*, **116**, 163910 (2014).
15) D. Eberbeck, F. Wiekhorst, S. Wagner, and L. Trahms: *Appl. Phys. Lett.*, **98**, 182502 (2011).
16) T. Yoshida, N. B. Othman, and K. Enpuku: *J. Appl. Phys.*, **114**, 173908 (2013).
17) S. Ota, R. Takeda, T. Yamada, I. Kato, S. Nohara, and Y. Takemura: *Int. J. Magn. Part. Imag.*, **3**, 1703003 (2017).
18) R. E. Rosensweig: *J. Magn. Magn. Mater.*, **252**, 370–374 (2002).
19) P. C. Fannin, C. N. Marin, C. Couper: *J. Magn. Magn. Mater.*, **322**, 1677–1681 (2010).
20) J. Carrey, B. Mehdaoui, and M. Respaud: *J. Appl. Phys.*, **109**, 083921 (2011).
21) K. D. Usadel: *Phys. Rev. B*, **95**, 104430 (2017).
22) H. Mamiya and B. Jayadevan: *Sci. Rep.*, **1**, 157 (2011).
23) T. Yoshida, S. Bai, A. Hirokawa, K. Tanabe, and K. Enpuku: *J. Magn. Magn. Mater.*, **380**, 105−110 (2015).
24) S. Ota, T. Yamada, Y. Takemura: *J. Appl. Phys.*, **117**, 17D713 (2015).
25) S. B. Trisnanto, S. Ota, and Y. Takemura: *Appl. Phys. Express*, **11**, 075001 (2018).
26) S. Ota and Y. Takemura: *Appl. Phys. Express*, **10**, 085001 (2017).
27) J. L. García-Palacios and F. J. Lázaro: *Phys. Rev. B*, **58**, 14937–14958 (1998).
28) L. Lopez-Diaz, L. Torres, and E. Moro: *Phys. Rev. B*, **65**, 224406 (2002).
29) E. C. Stoner and E. P. Wohlfarth: *Philos. Trans. R. Soc. London, Ser. A*, **240**, 599 (1948).
30) W. T. Coffey and Y. P. Kalmykov: Langevin equation 3rd ed., pp. 126–130 (World Scientific, Singapore, 2012).
31) W. T. Coffey and Y. P. Kalmykov: *J. Magn. Magn. Mater.*, **164**, 133–142 (1996).
32) T. Yoshida, Y. Matsugi, N. Tsujimura, T. Sasayam, K. Enpuku, T. Viereck, M. Schilling, F. Ludwing: *J. Magn. Magn. Mater.*, **427**, 162–167 (2017).
33) R. Takeda, S. Ota, T. Yamada, Y. Takemura: *J. Magn. Soc. Jpn.*, **42**, 55–61 (2018).
34) A. Sukhov and J. Berakdar: *J. Phys.: Condens. Matter*, **20**, 125226 (2008).
35) G. E. Uhlenbeck and L. S. Ornstein: *Phys. Rev.*, **36**, 823–841 (1930).
36) J. Carrey and N. Hallali: *Phys. Rev. B*, **94**, 184420 (2016).
37) T. Yoshida and K. Enpuku: *Jpn. J. Appl. Phys.*, **48**, 127002 (2009).

Received Oct. 11, 2018; Accepted Jan. 8, 2019

Editorial Committee Members・Paper Committee Members

Notice for Photocopying

編 集 委 員・論 文 委 員

複写をされる方へ

Journal of the Magnetics Society of Japan

Vol. 43 No. 2 (通巻第 302 号) 2019 年 3 月 1 日発行

Vol. 43 No. 2 Published Mar. 1, 2019
by the Magnetics Society of Japan
Tokyo YWCA building Rm207, 1–8–11 Kanda surugadai, Chiyoda-ku, Tokyo 101–0062
Tel. +81–3–5281–0106 Fax. +81–3–5281–0107

Printed by JP Corporation Co., Ltd.
Sports Plaza building 401, 2–4–3, Shinkamata Ota-ku, Tokyo 144–0054
Advertising agency: Kagaku Gijutsu-sha

発行：（公社）日本磁気学会 101–0062 東京都千代田区神田駿河台 1–8–11 東京YWCA会館 207 号室
製作：ジェイピーシー 144–0054 東京都大田区新蒲田 2–4–3 スポーツプラザビル401 Tel.（03）6715–7915
広告取扱い：科学技術社 111–0052 東京都台東区柳橋 2–10–8 武田ビル 4F Tel.（03）5809–1132